Environmental Science Advances

ROYAL SOCIETY OF CHEMISTRY

PAPER

View Article Online
View Journal | View Issue

Cite this: *Environ. Sci.: Adv.*, 2022, **1**, 121

The solvothermal synthesis of a 3D rod-like Fe–Al bimetallic metal–organic-framework for efficient fluoride adsorption and photodegradation of water-soluble carcinogenic dyes†

Arnab Mukherjee,[a] Prasanta Dhak[b] and Debasis Dhak *[a]

A thermally stable, 3D rod-like, nanosized, porous, pH-stable Fe–Al bimetallic metal–organic-framework with terephthalic acid (1,4-benzenedicarboxylic acid) as a linker (abbreviated to Fe–Al BDC) with a surface area of 120.255 $m^2\ g^{-1}$ was synthesized using a solvothermal method for fluoride adsorption and the photodegradation of rhodamine B (RhB)/methylene blue (MB) within a pH range of 2–11. The μ-oxo metal bonds and 3D rod-like structure of Fe–Al BDC were determined *via* PXRD, FTIR, Raman spectroscopy, and FESEM analyses. The relationship between the particle size and surface area obeyed the André relationship. The chemisorption of fluoride, supported by XPS and FTIR studies, obeyed pseudo-second-order kinetics, with a Langmuir/Freundlich adsorption isotherm, and thermodynamic studies were undertaken. RhB/MB (10^{-5}/10^{-4} M) photodegraded under solar irradiation following pseudo-first-order kinetics. The surface–boundary-layer fluoride adsorption mechanism is confirmed based on the interparticle-diffusion model and mass-transfer model supported by ξ-potential analysis, and the mineralization mechanism of RhB was established using Kröger–Vink notation and HPLC studies; the material was reusable for up to eight cycles.

Received 1st October 2021
Accepted 13th February 2022

DOI: 10.1039/d1va00019e

rsc.li/esadvances

Environmental significance

Due to urbanization and industrialization (fertilizers, steel industry, *etc.*), toxic elements like fluoride (F^-) and textile dyes, especially the carcinogenic non-biodegradable aromatic dye rhodamine B (RhB), are continuously polluting consumable water bodies. The chronic intake of this polluted water can lead to several health issues. To eliminate F^- and RhB, an eco-friendly method is needed. Herein, an Fe–Al bimetallic metal–organic framework (MOF) with 1,4-benzenedicarboxylic acid as an organic linker with a surface area of 120.255 $m^2\ g^{-1}$ has been synthesized using the solvothermal method. This MOF chemisorbed F^- obeying the interparticle-diffusion model and mass-transfer model (removal efficiency: 95.60%), photodegraded the water-soluble dye RhB (degradation efficiency: 99.61% for 10^{-4} M RhB) within a pH range of 2–11 using sunlight (a renewable source), and was reusable for up to eight cycles.

1. Introduction

The toxicity of metal-based nanomaterials[1] can be resolved/minimized *via* the utilization of long-known carbon materials[2] and metal–organic-frameworks (MOFs) have been known as a novel technique to overcome these technical limitations,[3] since MOFs have a high surface area, large pore volume, and an elegant topology.[4] Due to some natural (rock–water interaction, volcanic/tectonic processes, weathering, *etc.*) and anthropogenic sources (phosphate fertilizers, herbicides, steel, aluminum, glass, and tile industries),[5] consumable groundwater is continuously contaminated by fluoride (F^-) and the degree of usage of water-soluble dyes (*e.g.* methylene blue) in different industrial applications,[6] followed by continuous discharge, also affects water-bodies.

Adsorption is a promising method for defluorination as it has high removal efficiency, simple operation, and relative cost-effectiveness[7,8]. Some Al(III) containing materials, such as activated alumina,[9] alum impregnated activated alumina,[10] aluminum hydroxide soaked limestone,[11] and CaO modified activated alumina,[12] were applied for F^- adsorption as these adsorbent-surfaces are positively charged. The difficulties with these adsorbents are that they have a low surface area, which quickly gets saturated[13] and the adsorption is highly pH specific (only at pH ≤ 3.0)[7] so their use becomes expensive due to pH adjustment.

The aqueous-phase photodegradation of various toxic water-soluble organic dyes using sunlight, a freely available renewable light source under natural conditions, gives an additional advantage in the search for newer sustainable alternatives[14] to

[a]*Nanomaterials Research Lab, Department of Chemistry, Sidho-Kanho-Birsha University, Purulia-723104, India. E-mail: debasis.chem@skbu.ac.in; debasisdhak@yahoo.co.in*

[b]*Department of Chemistry, Techno India University, Kolkata–700091, India*

† Electronic supplementary information (ESI) available. See DOI: 10.1039/d1va00019e

partially/completely break down into relatively nontoxic constituents with lower hydrocarbons or end up with mineralization.[15] Trivalent metals (Al^{3+}, Cr^{3+}, and Fe^{3+}) in MOFs were used for the photodegradation of methylene blue under 500 W Xe lamp irradiation in the open air.[16] $CuWO_4$ modified MOF was applied to degrade 4-nitrophenol and methylene blue (MB) photocatalytically.[17] Cu(II) and Zr(IV) based MOFs were used to remove MB within the pH range 3–6,[18,19] and CdS/g-C_3N_4/MOFs were used to degrade rhodamine B (RhB) up to 90.20% under visible light.[20]

This present study is focused on the general properties of MOFs (*e.g.*, thermal and chemical stabilities, porous structures, high surface area), and a new kind of bimetallic MOF with Fe^{3+} and Al^{3+}, synthesized using 1,4-benzenedicarboxylic acid or terephthalic acid (BDC) as a linker in dimethylformamide (DMF) medium by a solvothermal method and abbreviated to Fe–Al BDC. Fe–Al BDC was used for the photodegradation of various water-soluble hazardous dyes (*e.g.*, RhB, [9-(2-carboxyphenyl)-6-(diethylamino)xanthen-3-ylidene]-diethylazanium chloride, and MB, 3,7-bis(dimethylamino)-phenothiazine-5-ium chloride) using solar irradiation and the efficient chemisorption of F^- in a different pH range (pH 2–11) for the first time to the best of our knowledge. The roles of temperature and reaction time in preparing Fe–Al BDC using the solvothermal process were investigated by varying these two parameters, keeping the reactant concentrations unchanged. The detection of the optimal conditions for the preparation was done by PXRD analyses of the synthesized materials under various conditions. The reusability of the solvent used in this synthesis was also checked. In this work, F^- removal and the photocatalytic nature of Fe–Al BDC were systematically investigated under various operating conditions, such as initial F^-/dye concentration, contact/reaction time, dose, solution pH, temperature, competing anions, reusability, and field water samples.

2. Materials and methods

The bimetallic nano-MOF Fe–Al BDC was prepared using a mixture of iron chloride ($FeCl_3 \cdot 6H_2O$, Merck India, Mumbai), aluminum nitrate ($Al(NO_3) \cdot 9H_2O$, ≥95%, Merck India, Mumbai), terephthalic acid (98%, Sigma-Aldrich), and *N*,*N*′-dimethylformamide (DMF) (≥99%, Merck India, Mumbai). All materials were of analytical grade and were used without further purification. 1 mmol of the metal salts and terephthalic acid were taken in 10 mL of DMF into a 100 mL Teflon-lined stainless-steel container and reacted at different temperatures (373 K, 423 K, and 473 K) for different heating times (24 h, 48 h, and 70 h, respectively). After cooling down, the solid was filtered using Whatman 42 and washed with methanol followed by drying in a hot-air oven for 1 h to obtain the final product. The entire synthesis course is depicted in Fig. 1. All of the instrumental information has been given in the ESI.

3. Results and discussion

3.1. Characterization

The optimum condition to synthesize Fe–Al BDC was 473 K for 70 h, which was confirmed by the PXRD analysis of these syntheses, as shown in Fig. 2a where the synthesized product Fe–Al BDC showed maximum PXRD peaks signifying the formation of phase-pure nano bimetallic MOF. The thermal stability of Fe–Al BDC was confirmed by TGA analysis (the TGA figure is not shown) where the synthesized MOF was thermally stable up to 300 °C. The XRD data showed that with an increase in reaction time and reaction temperature, the phase growth increased, which implies that the nucleation rate of the formation of nanoparticles was controlled by the temperature and reaction time in the precursor concentration.[21] These parameters increased the nucleation rate, leading to a smaller average grain size (nm), as shown in Fig.S4† revealed from the FESEM studies where the same concentration of the precursor was heated at 473 K for different reaction times (24 h, 48 h, and 70 h). The PXRD peaks of the MOF synthesized at 473 K for 70 h are matched with JCPDS file 84–2232 and it shows a monoclinic unit cell structure with space group (S.G) *C*2/*c*(15) and the average crystallite size of the MOF was 26.85 nm derived using Scherrer's equation $\left(D = \frac{0.9\lambda}{\beta \cos \theta}\right)$.[22,23] A Williamson–Hall (W–H) plot[24] was done (Fig. S5†) to calculate the crystalline strain (*e*), distortion density (δ), stacking fault (SF), unit cell parameters, crystallite size, and average cell volume (see Table S1†).

Fig. 2b shows the FTIR spectrum of the synthesized Fe–Al BDC and peaks at around 661 cm^{-1} and 590 cm^{-1} were observed, which denote the μ-oxo Fe_3O and Fe–O bonds in Fe–Al BDC, respectively,[25] which is also supported by the PXRD structure shown in Fig. S2 and S3.† A broad peak at 3407 cm^{-1} is attributed to the O–H stretching vibrations from surface-adsorbed water.[26] Bands at 1690–1404 cm^{-1} are for the asymmetric stretching of the metal-coordinated carboxylate group and the peak at 474 cm^{-1} represents C–H bending vibrations on the terephthalic acid linker,[27] as shown in Fig. 2b. The peaks in the 1690–1404 cm^{-1} region also represent the sp^2-hybridized C–H in-plane bending of the terephthalic acid linker aromatic rings,[26] as shown in Fig. 2b. The bands at 1334–890 cm^{-1} are for the asymmetric Al–O and symmetric Al–O bonds and the peaks at 837 cm^{-1} and 762 cm^{-1} are for the symmetric Al–O vibration,[28] as shown in Fig. 2b.

The Raman spectral analysis of Fe–Al BDC is shown in Fig. 2c, where the vibrations around 633 cm^{-1} and 920 cm^{-1} correspond to the benzene ring, and 1157 cm^{-1} and stretching at 1611 cm^{-1} represent the in-phase and out-of-phase vibrations of the –O–C=O group present in the terephthalic acid, respectively.[29] The presence of 1157 cm^{-1} and 1611 cm^{-1} Raman peaks for Fe–Al BDC also indicate the presence of sp^3 domains of carbon layers and sp^2 in-plane carbon vibrations *i.e.*, the D band and G band, respectively,[30] and the occurrence of the carbon centers in Fe–Al BDC was also supported by the FTIR and PXRD studies, as stated earlier.

Fig. 2d displays the UV-vis DRS of the synthesized Fe–Al BDC where high adsorption bands from 300 to 400 nm were observed for the ligand-to-metal charge transfer (LMCT), representing the bonding of carboxylate oxygen to the metals for the $^6A_{1g} \rightarrow {}^4A_{1g} + {}^4E_g(G)$ transition[31] and the presence of the metal-carboxylate

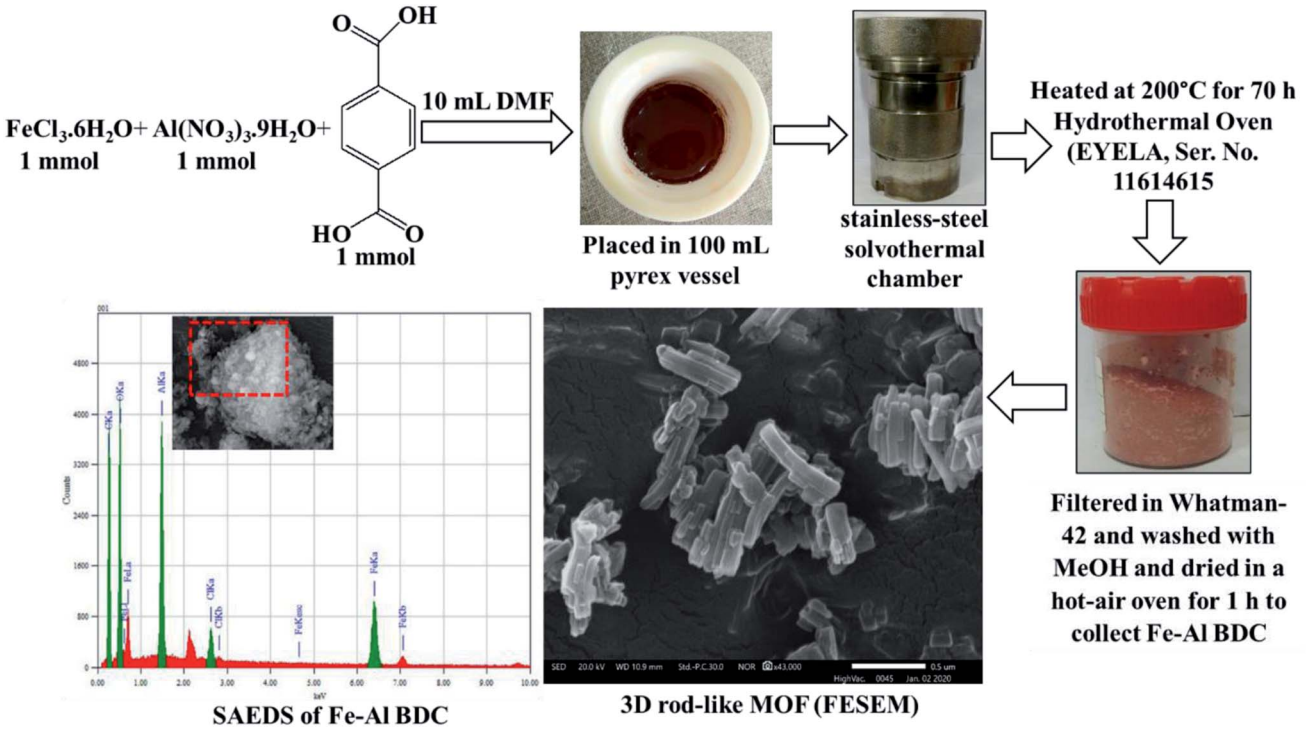

Fig. 1 Synthesis of the Fe–Al bimetallic 3D-rod-like MOF and FESEM and SAEDS studies after synthesis at 473 K for 70 h.

bonding in Fe–Al BDC was also confirmed by the PXRD studies, as stated earlier. A comparatively lower adsorption band was observed at 520–620 nm for the $^6A_{1g} \rightarrow {}^4T_{2g}$ transition due to the presence of Fe^{3+} in the material,[31] as shown in Fig. 2d. As the electronegativity of Al^{3+} is lower than that of Fe^{3+}, so more LMCT occurred in Fe–Al BDC, resulting in a high adsorption band in the 300–400 nm region[16,29], as shown in Fig. 2d. Tauc's method, $(\alpha h\nu)^2 = A(h\nu - E_g)$, where α is the absorption coefficient, h is the Planck constant, A is a material-related constant, and $h\nu$ is the photon energy,[24] was applied to the higher LMCT energy region *i.e.*, 300–400 nm. The room-temperature bandgap (E_g) of Fe–Al BDC prepared at 473 K for 70 h was calculated as 2.06 eV (Fig. 2d-inset), which was lower than that of the Fe-based MOF (E_g = 2.72 eV) reported by Jing-Jing Du *et al.*[16] Hence, the introduction of Al^{3+} into this newly synthesized MOF was expected to significantly contribute to enhancing the absorption by Fe–Al BDC in the visible-light region and improved photocatalytic activity by decreasing the E_g.

The surface morphology of Fe–Al BDC was estimated from the FESEM studies and the grains were 3D rod-like, as shown in Fig. S1c,† and the average grain size was calculated as 160 nm using UTI image tool software (version 3.0). Fig. S1d† shows the selected area energy dispersive X-ray study (SAEDS). Fig. 3(c–e) show the distributions of the elements (C, Fe, Al) and Fig. 3f shows the overlay of the distributions of the elements which were distributed homogeneously. Elemental analyses were also confirmed with an inductively coupled plasma mass spectrometer, using Thermo X-series II ICP-MS. The analysis was done using 0.01 g of Fe–Al BDC digested in 6 mL of aqua regia prepared from HNO_3 (70%) and hydrochloric acid (30%) in a Teflon tube, followed by microwave pressurization. The samples were heated to 260 °C for 10 min and then cooled, and the metals were quantified according to a standard curve and the data are given in Table S1.† The wt% of the metals present in the synthesized MOF Fe–Al BDC prepared at 473 K for 70 h were matched with the SAEDS results given in Fig. S1d-inset† and emphasized the formation of bimetallic Fe–Al BDC MOF with the same metallic proportions.

The effects of the precursor reaction temperature and reaction time on Fe–Al BDC were studied, following synthesis at different temperatures (373 K, 423 K, and 473 K) for different lengths of time. Fe–Al BDC formed at a higher temperature showed more phases, as shown in the PXRD study in Fig. 2a, and E_g increased with a decrease in the grain size, *i.e.*, the quantum confinement effect[21] was observed, as shown in Fig. S4.† Particles with an average size 26.13 ± 0.37 nm (23.77% polydispersity) and their distribution are shown in Fig. 3a and inset, respectively, for sample Fe–Al BDC prepared at 473 K for 70 h. HRTEM analysis indicates well-defined lattice fringes with an inter-planar distance (d) of 0.407 nm which corresponds to the (002) plane, as shown in Fig. 3a.

The activity of the synthesized nanoparticles, E_g, and the adsorption property are related to the surface area of the sample.[21] The BET isotherm of Fe–Al BDC is similar to a type IV isotherm with an H_3 type hysteresis loop, representing high adsorption at high relative pressure ($0.4 < P/P_0 < 1.0$),[32] as shown in Fig. 3b, with a surface area of 120.255 $m^2\ g^{-1}$. The pore diameter estimated from the Barrett–Joyner–Halenda (BJH) plot was found to be 1.3580 nm, as shown in Fig. 3b-inset. The bi-metallic MOF Fe–Al BDC prepared at 473 K for 70 h showed a 3D rod-like morphology compared to the others prepared at 373 K and 423 K for 70 h,

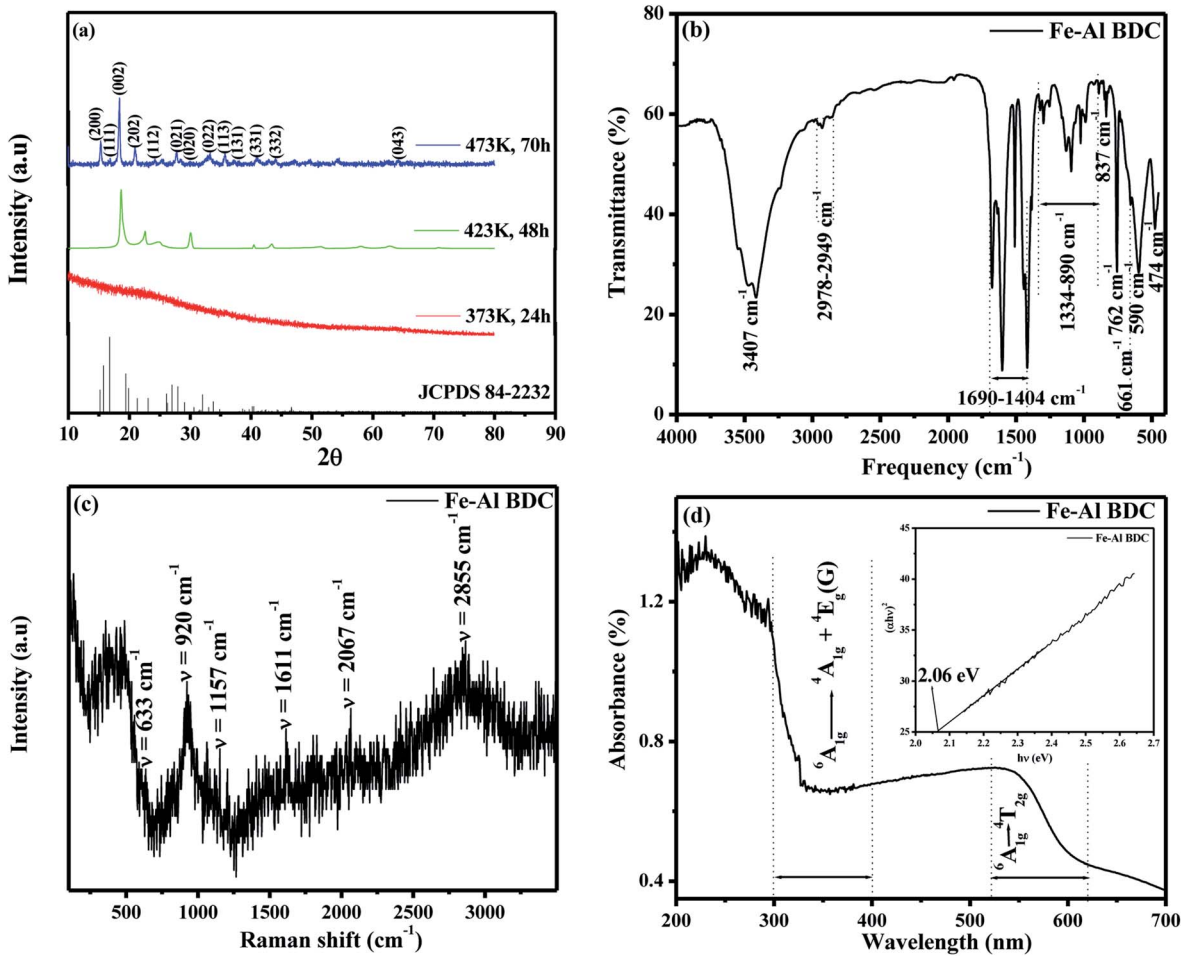

Fig. 2 (a) PXRD analysis (precursor heated to different temperatures of 373 K, 423 K, and 473 K for different heating times of 24 h, 48 h, and 70 h, respectively). (b) FTIR analysis, (c) Raman spectral analysis, and (d) the UV-vis DRS study of Fe–Al BDC prepared at 473 K for 70 h.

respectively, as shown in Fig. S1a–c.† Using PXRD and FESEM studies, the bi-metallic MOF Fe–Al BDC prepared at 473 K for 70 h is phase pure and has a good surface morphology. The surface area measurement of all materials (prepared at 373 K, 423 K, and 473 K for 70 h) along with the PXRD analysis (Fig. 2a) was undertaken and the particle sizes were correlated with the surface area, which obeyed the André *et al.*[33] relation, as shown in Fig. S6† (the details are in the ESI). As the particle size decreased, the surface area increased, obeying a linear pattern, as shown in Fig. S6,† and this study also supports the quantum confinement effect, as proposed by Lee *et al.*[21]

The photoluminescence (PL) spectrum of Fe–Al BDC excited at $\lambda = 300$ nm at room temperature is shown in Fig. S7.† Upon excitation, small humps at 428 nm for violet emission, at 494 nm and 458 nm for blue emission, and at 521 nm for green emission were observed[34] for Fe–Al BDC, as shown in Fig. S7.† The PL property of Fe–Al BDC gave rise to many oxygen vacancies, Farbe centers (F centers), metal vacancies, and carbon vacancies due to the large surface area,[35] and the crystal defects were also estimated from the W–H plot (see Fig. S5 and Table S1†). The vacancies formed in Fe–Al BDC were further explained with Kröger–Vink notation,[36] as shown in eqn (1)–(3).

$$\text{Fe} - \text{Al BDC} \leftrightarrow \text{Fe} - \text{Al BDC}_{4-n} + \frac{n}{4}\text{O}_2(\text{g}) \quad (1)$$

$$\text{Fe} - \text{Al BDC} \leftrightarrow \text{V}''_{\text{Fe-Al BDC}} + \text{V}^{\bullet}_{\text{O}} + \text{O}^{\bullet}_{\text{O}} \quad (2)$$

$$\text{V}^{\bullet}_{\text{O}} \leftrightarrow \text{V}^{\bullet\bullet}_{\text{O}} + \text{e}^- \quad (3)$$

where $\text{V}^{\bullet}_{\text{O}}$, $\text{V}^{\bullet\bullet}_{\text{O}}$, $\text{O}^{\bullet}_{\text{O}}$, and e^- correspond to a neutral oxygen vacancy, singly ionized oxygen vacancy, oxide in a lattice site, and the presence of an electron in the CB, respectively.

The defects and various point defects of the synthesized Fe–Al BDC prepared at 473 K for 70 h were detected *via* the W–H plot and PL spectral analyses. This fact was further confirmed by the EPR analysis, as shown in Fig. 4, where the spectrum consists of three distinct signals *i.e.*, signal I, signal II, and signal III, indicating the paramagnetic nature of the material.[34] Signal I and signal III are weaker signals in the lower magnetic field region and the higher magnetic field region, respectively, and signal II appeared in a moderately higher magnetic field region which is strongly suggestive of bulk surface defects[37,38] generating the paramagnetic nature.[34] Signal II consists of a quartet signal, as clearly shown in Fig. 4-inset, indicating the paramagnetic nature arising due to Fe^{3+}-d^5 (ref. 39) and Al^{3+}-d^0 (ref. 40) metal ions

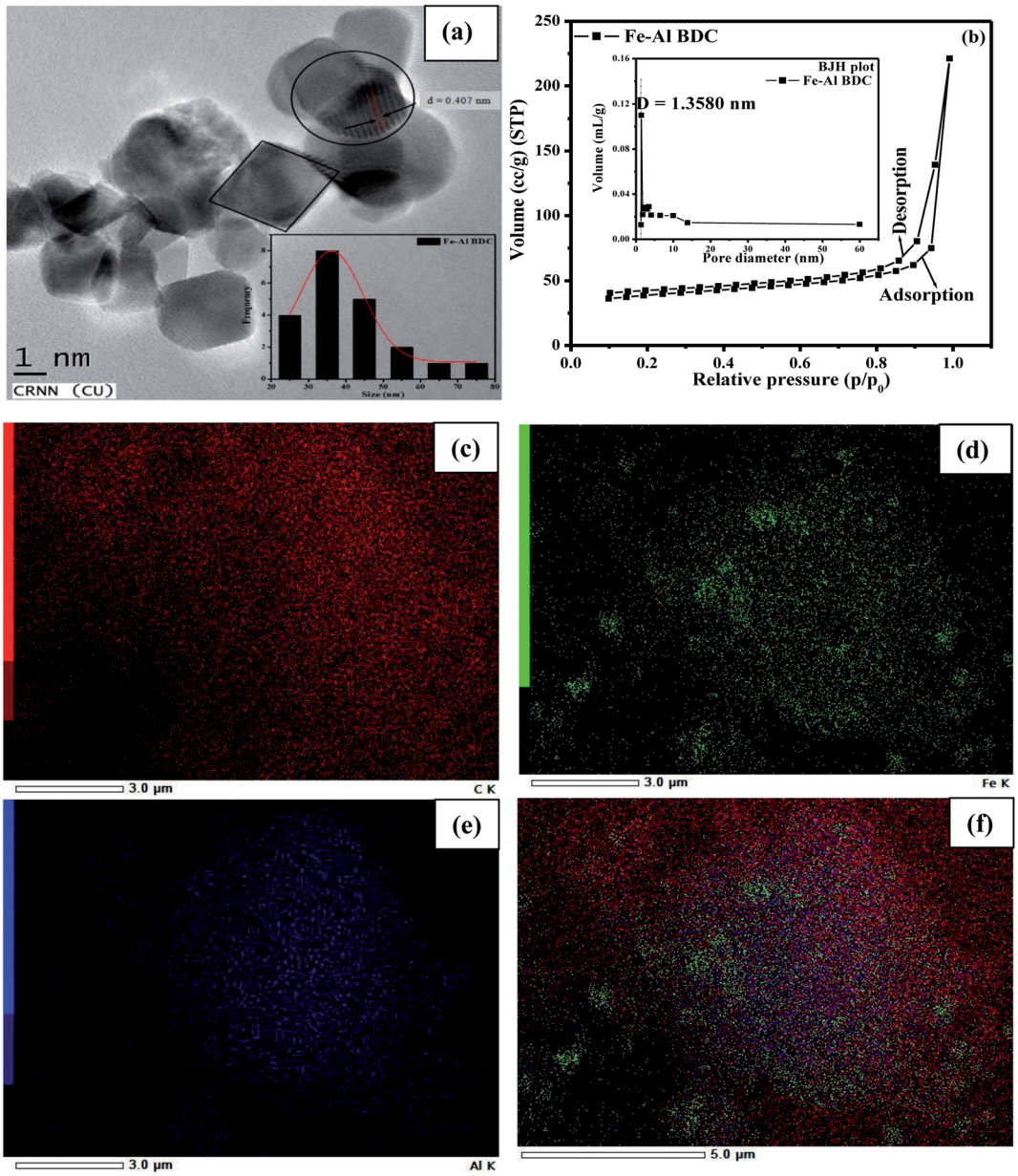

Fig. 3 (a) HRTEM analysis (lattice fringes are shown in the circular area, and inset – the distribution of particle sizes from TEM analysis), (b) nitrogen adsorption/desorption isotherm (inset – pore size distribution-BJH method), and elemental mapping showing (c) C, (d) Fe, and (e) Al and (f) overall elemental mapping in Fe–Al BDC prepared at 473 K for 70 h.

present in Fe–Al BDC, which is also supported by the XPS analysis, as shown in Fig. 9A-a. This quartet signal also signifies the presence of Fe^{3+}-d^5 and Al^{3+}-d^0 metal ions in the MOF system giving rise to singly ionized oxygen vacancies,[40] which was also supported by the PL spectra and eqn (2) and (3). The generation of the oxygen vacancies may enhance the photocatalytic nature of Fe–Al BDC and the photodegradation of dyes, which may be influenced by the generation of $OH^{\bullet}$ radicals in an aqueous medium.[34]

3.2. Fluoride adsorption and photodegradation studies

The overall F^- adsorption study was performed using a previously reported method[22] with different concentrations of initial F^- solutions prepared from 1000 mL of 1000 ppm F^- stock solution (2.0 g of NaF dissolved in 1000 mL of double distilled water); 3 ppm, 5 ppm, and 10 ppm F^- solutions were exposed to batches of 0.05, 0.10, and 0.15 g/100 mL Fe–Al BDC prepared at 473 K for 70 h, varying the contact time from 15 to 60 min using an orbital shaker (Theta, RPM-0249 TXT-7203, Paragon, India) at 30 °C and pH 7. The adsorbents were removed using a centrifuge with 150 spm (shakes per minute) and F^- detection was done using a Thermo Scientific (Orion Versasatar) electrochemistry meter.[41] The results for different initial F^- concentrations concerning different adsorbent doses and contact times have been tabulated in Table S3† and the variation in the % F^- removal with the variation in adsorbent dose and contact time are shown in Fig. S8 and S9,† respectively. From the Table

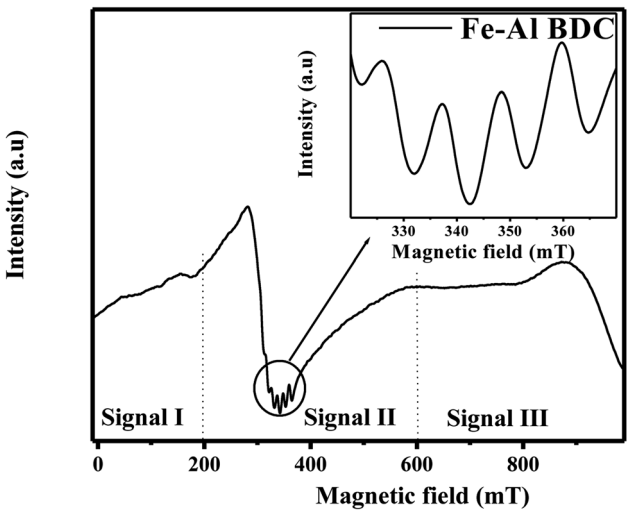

Fig. 4 The EPR spectrum of Fe–Al BDC (inset – quartet signal) at room temperature prepared at 473 K for 70 h.

S3† data, it was observed that Fe–Al BDC with a 0.10 g/100 mL adsorbent dose with 45 min contact time showed the highest removal efficiency: *i.e.*, 95.60% for the 10 ppm initial F^- solution at 30 °C, pH 7. To find out the saturation time, the contact time was varied from 5 to 300 min using different initial F^- solutions (10 ppm, 20 ppm, 30 ppm, 40 ppm) using 0.10 g/100 mL Fe–Al BDC prepared at 473 K for 70 h at 30 °C, pH 7, and the saturation time was found to be 45 min, as shown in Fig. 5a. After 45 min contact time, F^- removal efficiencies were highest for all the F^- solutions and after that the removal efficiencies slightly decreased and the adsorption equilibrium was established, as shown in Fig. 5a. This happened due to the kinetically controlled adsorption[24,42] of overpopulated F^- ions onto the active sites of the Fe–Al BDC adsorbent. As the time elapses, dissolution due to repulsions among the adsorbed F^- ions starts[42] which is reflected in the decreased removal efficiency values after 45 min contact time, as shown in Fig. 5a.

As 0.10 g/100 mL Fe–Al BDC showed maximum efficiency for the F^- adsorption studies, the same dose of Fe–Al BDC was applied for the photodegradation studies with 100 mL of different concentrations (10^{-5} M/10^{-4} M) of a xanthene class of dye, RhB, and a thiazine class of dye, MB, taken in a 250 mL beaker and kept in the dark for 30 min to achieve adsorption–desorption equilibrium. Then the mixture was exposed to sunlight with occasional stirring under ambient conditions

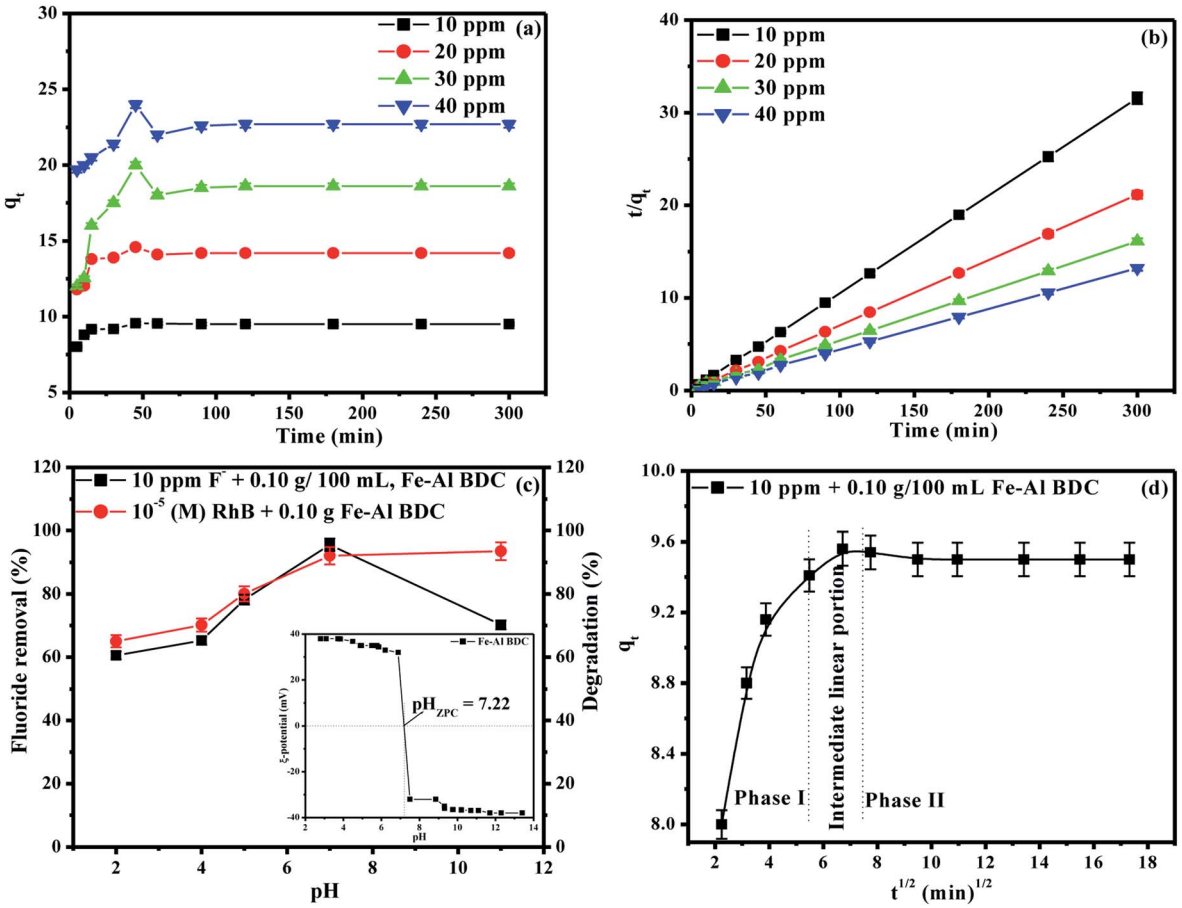

Fig. 5 (a) Non-linear kinetic plots of F^- adsorption, (b) pseudo-second-order kinetic plots of F^- adsorption using 10 ppm, 20 ppm, 30 ppm, and 40 ppm initial F^- solutions, (c) a pH variation study of F^- adsorption using 10 ppm initial F^- solution and the photodegradation of 10^{-5} M RhB (inset: the ξ-potential study of Fe–Al BDC), and (d) the intra-particle diffusion (IPD) study of F^- adsorption using 10 ppm initial F^- solution with 0.10 g/100 mL Fe–Al BDC (at 30 °C, pH 7 for F^- removal studies and at pH 7 for the photodegradation studies) prepared at 473 K for 70 h.

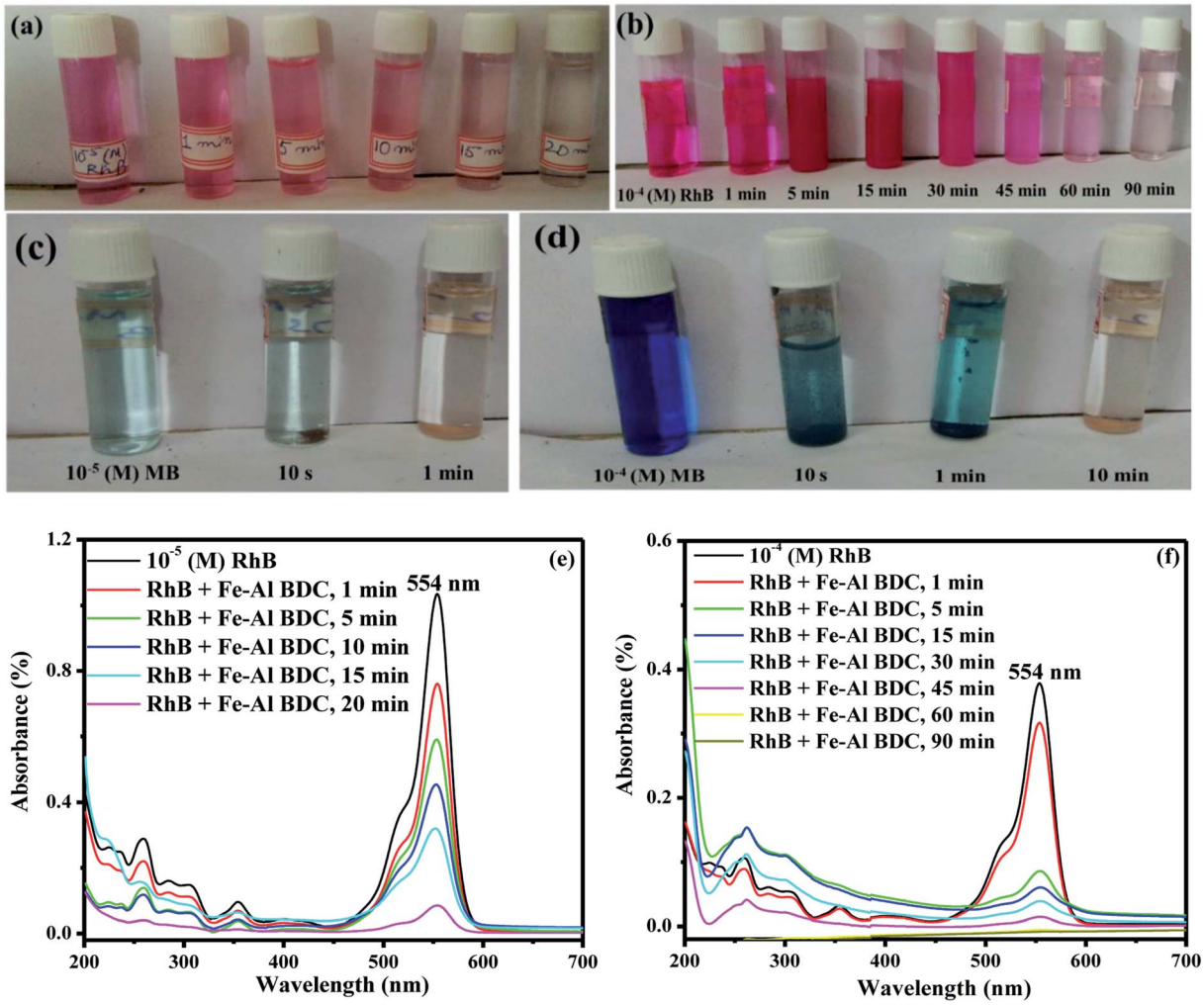

Fig. 6 Photographs of vials: (a) 10^{-5} M RhB, (b) 10^{-4} M RhB, (c) 10^{-5} M MB, and (d) 10^{-4} M MB. UV-vis spectral analysis of the photodegradation of (e) 10^{-5} M RhB and (f) 10^{-4} M RhB with a change in solar irradiation time for 0.10 g/100 mL Fe–Al BDC prepared at 473 K for 70 h at pH 7.

between 10:00 am and 4:00 pm (latitude and longitude of 23.3613°N, 86.3399°E respectively, in the month of April, Purulia, West Bengal, India) with an average solar intensity of 6.08 kW h m^{-2} following a previously reported method.[24] The synthesized Fe–Al BDC prepared at 473 K for 70 h was a better F^- adsorbent as well as a photocatalyst for the degradation of RhB/MB than previously reported MOFs when comparing time and efficiency, as shown in Tables 2A and B, respectively.

The arrested solutions in the photodegradation of $10^{-5}/10^{-4}$ (M) RhB/MB solutions using 0.10 g/100 mL Fe–Al BDC are shown in Fig. 6a–d and the UV-Vis spectroscopic data are shown in Fig. 6e, f, S11a and b,† respectively. The change in concentration of RhB with respect to solar-irradiation time is shown in Fig. 7a.

3.3. Kinetics of fluoride adsorption and dye degradation

The kinetic measurements of the F^- removal efficiencies of different initial F^- solutions (3 ppm, 5 ppm, 10 ppm) for different contact times (15–60 min) using different adsorbent doses of Fe–Al BDC (0.05–0.15 g/100 mL) at 30 °C, pH 7 were taken and the results are tabulated in Table S3† and shown in Fig. S10a–c.† The F^- adsorption followed the pseudo-second-order kinetic model $\left(q_t = \frac{t}{\frac{1}{q_e^2 k_2} + \frac{t}{q_e}}\right)$[41] and the pseudo-second-order rate constant (k_2 g min mg^{-1}) was estimated using the $\frac{t}{q_t}$ *vs.* t (min) plot and the highest value of k_2 was found for the 10 ppm initial F^- solution with 0.10 g/100 mL adsorbent dose of Fe–Al BDC ($k_2 = 1.076 \times 10^{-1}$ g min mg^{-1}). The saturation time was 45 min from the non-linear kinetic plot, as shown in Fig. 5a. The contact time varied from 5 to 300 min and F^- adsorption studies were done for 10 ppm, 20 ppm, 30 ppm, and 40 ppm initial F^- solutions, and the kinetic results are shown and tabulated in Fig. 5b and Table 1, respectively, at 30 °C, pH 7.

The change in concentrations of $10^{-5}/10^{-4}$ (M) RhB and MB with variation in the solar-irradiation time are shown in Fig. 7a, and S13a† for $10^{-5}/10^{-4}$ (M) RhB and Fig. S12a, and in

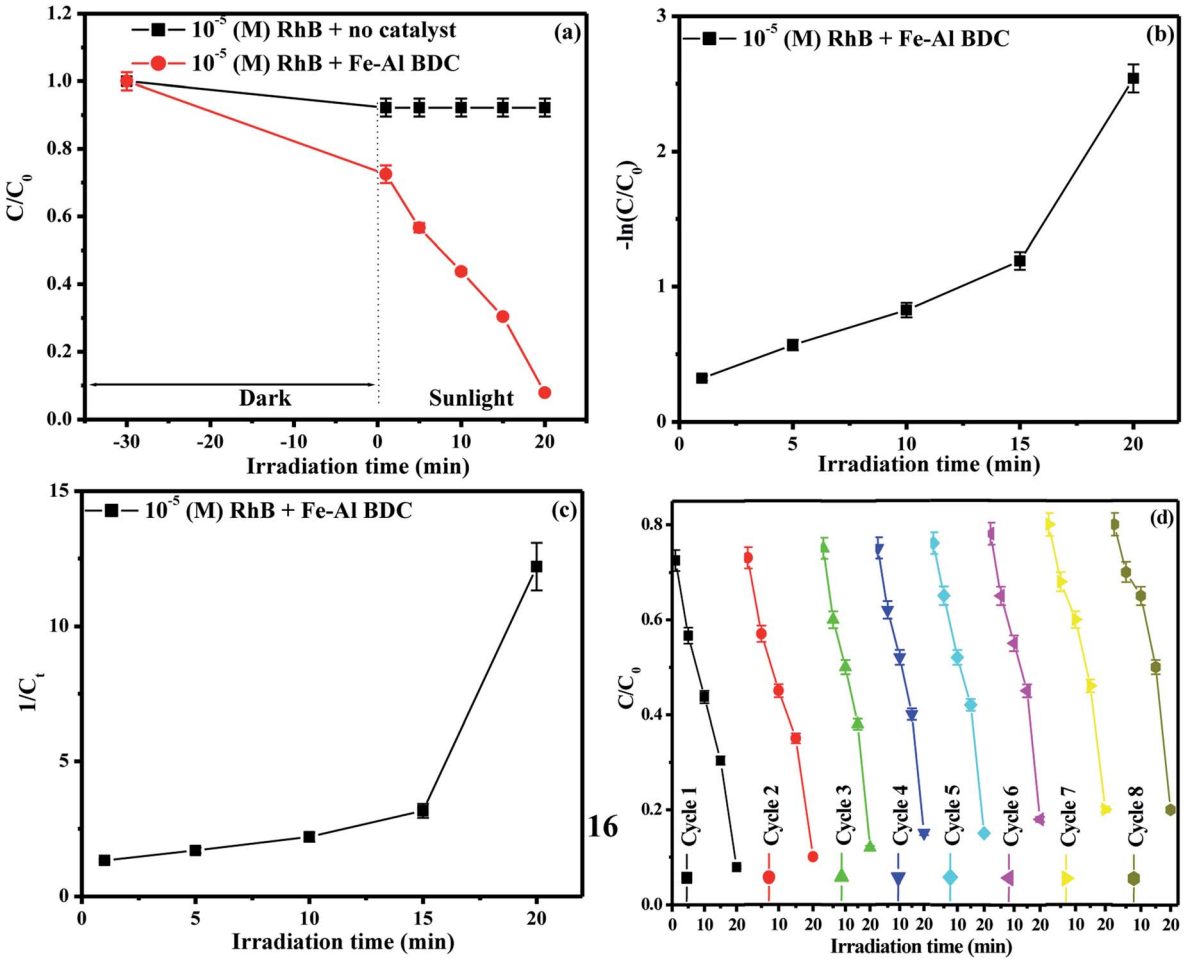

Fig. 7 (a) Variation in concentration with a change in the solar irradiation time, (b) pseudo-first-order and (c) pseudo-second-order kinetics studies, and (d) a reuse study for the photodegradation of 10^{-5} M RhB using 0.10 g of Fe–Al BDC prepared at 473 K for 70 h at pH 7.

Fig. S11c† for $10^{-5}/10^{-4}$ (M) MB, respectively. For the kinetic studies of the dye photodegradation process, both the Lindemann–Hinshelwood pseudo-first-order $\left(-\ln\frac{C}{C_0} = k_1 t\right)$[43] and pseudo-second-order kinetic model $\left(\frac{1}{C_t} = k_2 t + \frac{1}{C_0}\right)$[44] were checked and the data are tabulated in Table 1. The kinetic plots are shown in Fig. 7b, c, S13b and c† for $10^{-5}/10^{-4}$ (M) RhB and Fig. S12c–d and Fig. S11c-inset† for $10^{-5}/10^{-4}$ (M) MB photodegradation, respectively. It can be seen that the kinetics of photodegradation of RhB/MB under solar irradiation using Fe–Al BDC was more dominated by pseudo-first-order kinetics than by pseudo-second-order as the regression coefficients (R^2) were closer to unity for the pseudo-first-order results, as shown in Table 1.

3.4. pH, co-ions, reuse, and field water sample studies

The solution pH is one of the major factors affecting the adsorption capacity or any other reaction taking place in the solution phase[7] and to investigate the influence of the solution pH on F^- adsorption and the photodegradation of organic dyes (RhB/MB) by Fe–Al BDC, tests were performed in pH 2–11 using 10 ppm initial F^- solution and 10^{-5} (M) RhB with 0.10 g/100 mL Fe–Al BDC, as shown in Fig. 5a. The pH of the solution was regulated using 0.1 (M) HCl and 0.1 (M) NaOH solutions. The pH_{ZPC} of Fe–Al BDC was 7.22, as shown in Fig. 5a-inset. In the acidic situation *i.e.*, pH < pH_{ZPC}, the interaction between the H^+ ions present in the solution and the Fe–Al BDC surface becomes greater, and in the alkaline medium the interaction with the OH^- ions increases. At pH > pH_{ZPC} the surface is negatively charged and at pH < pH_{ZPC} the surface becomes positively charged.[51] The F^- removal efficiency of Fe–Al BDC increased with an increase in the solution pH from 2 to 7 and decreased at higher pH, *i.e.*, pH 11, as in the lower pH the interaction/repulsion with the positively charged surface increased with more H^+ ions present in the solution, and *vice versa* for higher pH with OH^- and the negatively charged surface, as shown in Fig. 8a showing the surface–boundary-layer mechanism using the electrophoretic mobility model[41] discussed previously. At pH 7, the F^- removal efficiency of Fe–Al BDC was greater (~95.60%) as the pH_{ZPC} of Fe–Al BDC was 7.22 (Fig. 5c -inset).

The photodegradation of 10^{-5} (M) RhB using 0.10 g/100 mL Fe–Al BDC in the pH range 2–11 is shown in Fig. 5c. The outcomes showed that the degradation efficiency of RhB using

Table 1 Pseudo-second-order, Weber and Morris, and thermodynamic parameter values for different initial F^- concentrations and the kinetics of dye degradation using 0.10 g/100 mL Fe–Al BDC prepared at 473 K for 70 h at 30 °C and pH 7

C_0 (ppm)	F^- removal %	k^2 (g min mg^{-1}) ($\times 10^{-1}$)	R^2
10	95.60	1.07	0.999
20	71.00	1.23	0.999
30	66.66	0.27	0.999
40	60.00	0.35	0.999

Weber and Morris intra-particle diffusion (IPD) model

	k_{ip} (mg g^{-1} $min^{0.5}$)		R^2	
C_0 (ppm)	$k_{ip}1$	$k_{ip}2$	$k_{ip}1$	$k_{ip}2$
10	0.428	−0.0027	0.911	0.621

Thermodynamic parameters

C_0 (ppm)	T (K)	ΔG^0 (kJ mol^{-1})	ΔH^0 (kJ mol^{-1})	ΔS^0 (J mol^{-1})
10	303	−50.38	−94.66	−147.50
	318	−48.38		
	328	−48.22		

Kinetics studies of dye degradation

Dye	C_0 (M)	Degradation %	k_1	R^2	k_2	R^2
RhB	$10-^5$	92.11	0.078 min^{-1}	0.957	0.146 L mol^{-1} min^{-1}	0.565
	10^{-4}	99.61	0.072 min^{-1}	0.937	1.059 L mol^{-1} min^{-1}	0.635
MB	10^{-5}	97.47	0.0307 s^{-1}	0.952	0.618 L mol^{-1} s^{-1}	0.859
	10^{-4}	99.19	0.007 s^{-1}	0.835	0.017 L mol^{-1} s^{-1}	0.783

Fe–Al BDC composite improved with an increase in pH, *i.e.*, alkaline pH, as shown in Fig. 5c. The change in the solution pH significantly affects the photodegradation of the dye, probably depending especially on two factors: firstly, the surface charge of the Fe–Al BDC (pH_{ZPC}) and secondly the pKa of the target, *i.e.*, RhB in solution.[52] The pKa value of RhB is 3.7 and thus the cationic form (RhB^+) exists in acidic pH and at higher pH a zwitterionic form ($RhB^{\pm}$) exists due to deprotonation of the carboxyl group.[53] As in the acidic environment, the RhB dye is in its cationic form and due to the high abundance of H^+ ions in the medium, the repulsion between the dye and the positively charged Fe–Al BDC surface became higher, leading to a decrease in the photodegradation percentage. In the basic medium, the enhancement in degradation is due to the effective interaction of $RhB^{\pm}$ and the negatively charged Fe–Al BDC surface through the positive side (positive charge on the nitrogen) of $RhB^{\pm}$(ref. 54) in the presence of more $OH^•$ radicals in the alkaline medium.[52] A schematic representation of RhB degradation is shown in Fig. 8b, describing the surface–boundary-layer mechanism. The same pH-dependent investigation was reported by Saleh *et al.*[52] for RhB photodegradation using tungsten oxide modified multiwalled carbon nanotubes and 50 mL of 10^{-5} (M) RhB aqueous solution. The % degradation of RhB was 92.11% at pH 7 and the degradation time was also less than for other pH media when the pH_{ZPC} of Fe–Al BDC was 7.22 (Fig. 5c-inset).

The disadvantage of the use of various adsorbents for F^- adsorption over a wide pH range is the interference with F^- ions by rival-anions/co-ions, such as chloride (Cl^-), sulfate (SO_4^{2-}), bicarbonate (HCO_3^-), nitrate (NO_3^-), and phosphate (PO_4^{3-}), in the solution[55] which are mainly also found in groundwater[56] and there are large amounts of NO_3^-, SO_4^{2-}, and Cl^- present in the wastewater of textile/dye industries.[57] In recent years, porous compounds such as MOFs with high porosity have been frequently chosen for F^- removal in the presence of interfering co-ions[58] and to degrade water-soluble colored wastes.[59] To check the effect of these co-ions on F^- adsorption, studies were undertaken using two sets of 10 ppm aqueous NaF solutions, one containing Cl^-, NO_3^-, and SO_4^{2-} and another containing Cl^-, NO_3^-, SO_4^{2-}, PO_4^{3-} and HCO_3^- of sodium salts as per the permissible limit of WHO at 30 ± 2 °C using a previously reported method.[24] For the photodegradation studies, 0.01 (M) NO_3^-, SO_4^{2-}, and Cl^- of the corresponding sodium salts were mixed into the 10^{-5} (M) RhB solution. In both experiments 0.10 g/100 mL Fe–Al BDC was used and in both cases the effect of Na^+ was neglected.[60] In Fig. S15a† the percentage of F^- removal was lowered from 82% to 75% in the presence of PO_4^{3-} and HCO_3^- along with the other anions rather than in the presence of Cl^-,

Table 2 A comparison of (A) F^- removal and (B) the photodegradation of dyes (RhB/MB) using other reported MOFs with Fe–Al BDC prepared at 473 K for 70 h

Serial no	Sample: Composite	Amount	Conc.	Efficiency	Time	Ref.
(A) Fluoride adsorption						
1	Sn(II)-benzene-1,3,5-tricarboxylic acid MOF	1.6 mg L^{-1}	12 ppm, F^-	~84%	150 min	45
2	Al-1,3,5-BTC MOF	0.5 g L^{-1}	10 ppm, F^-	95%	20 min	7
3	Al-fumarate MOF	0.75 g L^{-1}	30 ppm, F^-	~99.99%	24 h	13
4	Zr-containing UiO-66 MOF	0.01 g/20 mL	50 ppm, F^-	90% (20 °C)	30 min	46
5	MOF-801-Zr-fumarate MOF	1.5 g L^{-1}	10 ppm, F^-	91.80%	120 min	47
6	UIO-66 (Zr-1,4-benzenedicarboxylate MOF)	0.25 g L^{-1}	10 ppm, F^-	92.30%	60 min	48
7	Fe–Al BDC	0.10 g/100 mL	10 ppm, F^-	95.60%	45 min	This work
(B) Photodegradation of dyes (RhB/MB)						
8	CdS/g-C_3N_4/MOF	0.5 g L^{-1}	10 ppm RhB	90.20%, using visible light irradiation	90 min	20
9	Zn-BTC MOF	2 mg/50 mL	10 ppm, RhB[a], MB[b] mixed with H_2O_2 (100 mM)	85%[a], 79%[b], using visible light irradiation	90 min	49
10	3D MOF $[Cu(4,4'\text{-bipy})Cl]_n$	4 mg/50 mL	10 ppm, MB	93.93%, using visible light irradiation	150 min	50
11	Fe–Al BDC	0.10 g/100 mL	10^{-5} (M) RhB	92.11% using solar irradiation	20 min	This work
			10^{-4} (M) RhB	99.61% using solar irradiation	90 min	
			10^{-5} (M) MB	97.47% using solar irradiation	1 min	
			10^{-4} (M) MB	99.19% using solar irradiation	10 min	

NO_3^-, and SO_4^{2-}, as F^- follows the order $HCO_3^- < PO_4^{3-} < Cl^- \approx SO_4^{2-} < NO_3^-$[56] due to the pH effect[61] in the presence of PO_4^{3-} and HCO_3^- co-ions, as discussed previously.[24] The competition between F^- and OH^- along with the other ions increased at the active sites of the adsorbent Fe–Al BDC, *i.e.*, the Fe^{3+} and Al^{3+} (hard center). In the presence of the carbon centers, the borderline center helped the active sites specific to F^- in the presence of co-ions. In Fig. S15a† the photodegradation of RhB in the presence of the co-ions is shown, where the degradation decreased in the presence of Cl^- and SO_4^{2-} due to an increase in competition with RhB for the Fe–Al BDC surface and the pH factor of the solution, as discussed previously in this section. The degradation increased in the presence of NO_3^- which was discussed in the mechanism section of RhB degradation. In the presence of the co-ions, for the photodegradation process the degradation % varied as well as the degradation time also being prolonged (it required 60 min for complete decolorization; UV profiles not shown) compared to degradation without co-ions using 0.10 g/100 mL Fe–Al BDC under solar irradiation.

For the reuse studies of the re-collected Fe–Al BDC after F^- adsorption and photodegradation, a standard process was adopted[41] for $10^{-5}/10^{-4}$ (M) RhB/MB and it was re-useable in studies up to eight successive cycles, as shown in Fig. S18, 7d, S13d, and S12d,† respectively.

To check the selective adsorption of F^- by Fe–Al BDC in practical applications, some field water samples containing a significant amount of F^- were collected from the local area (latitude and longitude of 23.3613°N, 86.3399°E, respectively) and the detailed water analyses before and after treatment with Fe–Al BDC are given in Table S5† in the ESI. The presence of Cl^-, NO_3^-, SO_4^{2-}, PO_4^{3-} and HCO_3^- along with the F^- content were checked before and after treatment. Table S5† shows that the adsorption capacity of F^- onto Fe–Al BDC taking all four field water samples (F1, F2, F3, and F4) into account was ~95% in the presence of all the stated co-ions.

3.5. Adsorption isotherms and thermodynamics studies of fluoride adsorption

Adsorption isotherm studies were performed using 0.10 g/100 mL Fe–Al BDC for a 10 ppm initial F^- solution with the Langmuir[24] and Freundlich isotherm[62] models with regression coefficient (R^2) values of 1 and 0.955, respectively, and the Freundlich coefficient was $n = 1$, as shown in Fig. S15c and d,† respectively. The data were best fitted by the Langmuir model and using this model the values of Gibbs free energy (ΔG^0 kJ mol^{-1})) were evaluated for the corresponding temperatures, as stated in Table 1 using a previously reported method.[24] A thermodynamic study of F^- removal was

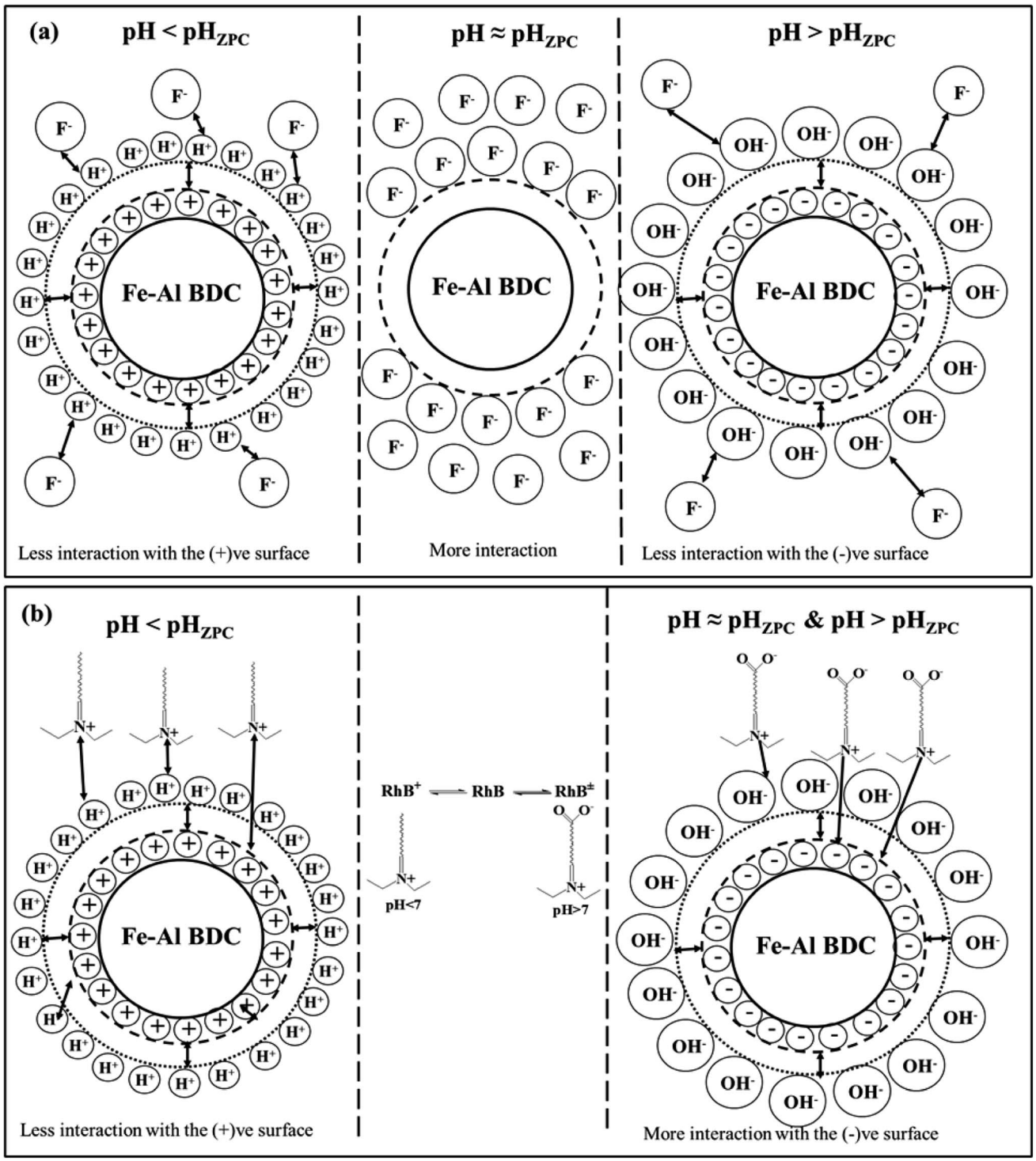

Fig. 8 A schematic representation of the surface–boundary-layer mechanism using the electrical double layer model for (a) F^- adsorption and (b) the photodegradation of RhB in different pH media onto an Fe–Al BDC surface prepared at 473 K for 70 h.

undertaken by varying the solution temperature (303, 318, 328 K) and the results obeyed the Van't Hoff equation $\left(\ln K = \frac{\Delta S^0}{R} - \frac{\Delta H^0}{RT}\right)$,[41] as shown in Fig. S15b† using 0.10 g/100 mL Fe–Al BDC for a 10 ppm initial F^- solution, and the results are stated in Table 1 where all the thermodynamic parameters (ΔG^0, ΔH^0, and ΔS^0) are negative showing that the adsorption process was exothermic, reversible and reusable.[24]

3.6. Mechanism

3.6.1. Mechanism of fluoride adsorption. F^- adsorption onto an adsorbent generally occurs *via* a three-step

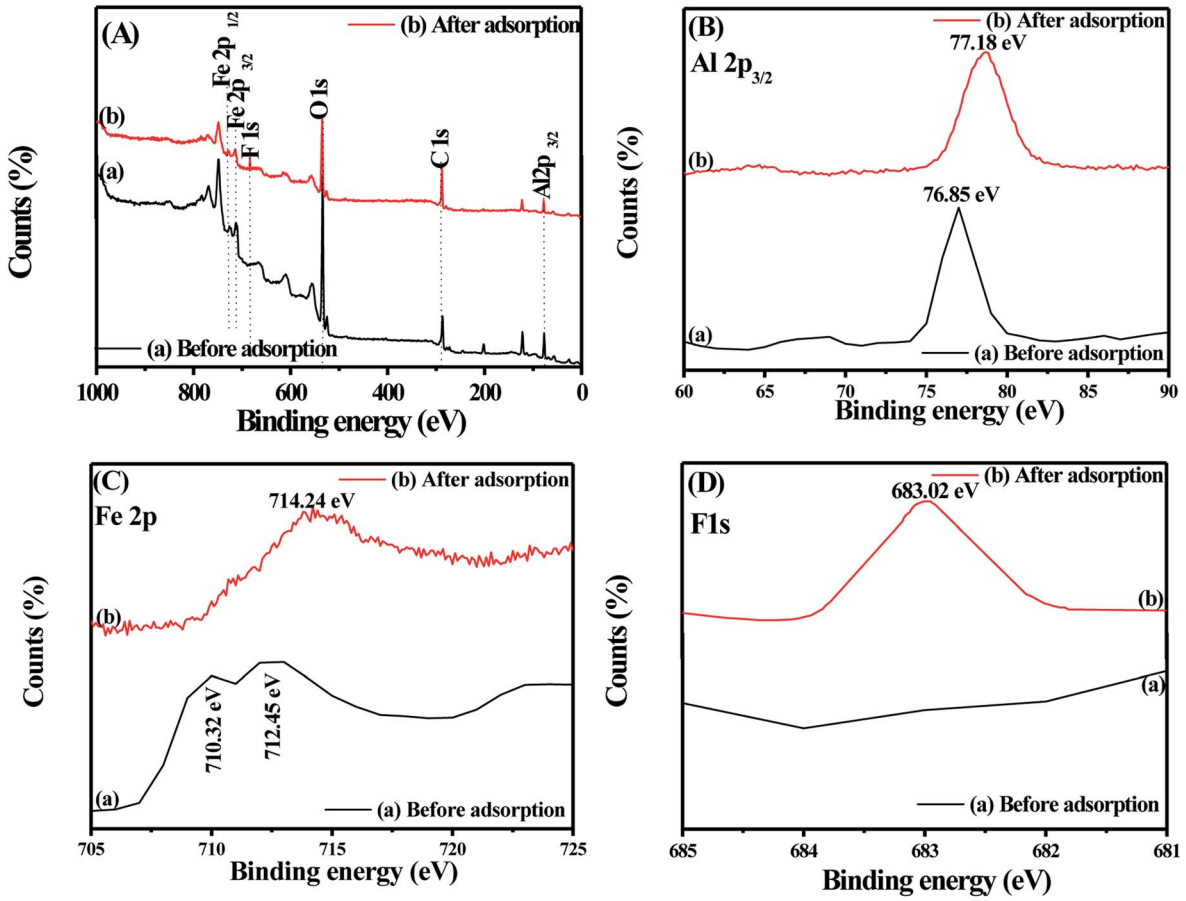

Fig. 9 XPS spectra of (A) (a) Fe–Al BDC prepared at 473 K for 70 h and (b) fluoride-adsorbed Fe–Al BDC prepared at 473 K for 70 h; (B) Al $2p_{3/2}$ area analysis (a) before fluoride adsorption and (b) after fluoride adsorption; (C) Fe $2p_{3/2}$ area analysis (a) before fluoride adsorption and (b) after fluoride adsorption; and (D) F 1s area analysis (a) before fluoride adsorption and (b) after fluoride adsorption at pH 7.

mechanism:[63] *i.e.*, (i) mass-transfer across the external boundary layer;[64] (ii) adsorption on the surface (internal or external), *i.e.*, physical or chemical adsorption depending on the ΔH^0 value (ΔH^0 > 10 kJ mol^{-1} for chemisorption);[65] (iii) diffusion of the adsorbate molecules onto the solid surface of the adsorbent.[7] Fe–Al BDC is a typically porous MOF with a large surface area, as confirmed from the BET surface studies, as shown in Fig. 3b. From the thermodynamics studies, ΔH^0 was found to be −94.66 kJ mol^{-1} and the FTIR studies of the used Fe–Al BDC confirmed the occurrence of the chemisorption process, as shown in Fig. S15b and S16,† respectively. The adsorbent got saturated after the 45 min contact time, as confirmed by the non-linear kinetic plot shown in Fig. 5a. To find out the velocity of F^- transport from the liquid phase to the Fe–Al BDC surface over this wide range of performed contact time (5–300 min), the mass-transfer kinetic model[64] and Weber and Morris intra-particle diffusion (IPD) model ($q_t = K_{ip}t^{1/2} + C$)[7] were applied, as shown in Fig. S14 and 5d,† respectively. For the mass-transfer kinetic model, the overall data (5–300 min contact time) is shown in Fig. S14a† where two phases were observed. Fig. S14b† shows the adsorption up to 45 min and Fig. S14c† shows the adsorption up to 300 min, which is very much parallel to the time axis describing the saturation. From Fig. S14b† the value of the mass-transfer-coefficient β_L was calculated from the slope of the linear–fit plot and was found to be 1.56×10^{-4} cm min^{-1}, which indicates that the velocity of F^- transport from the liquid phase to the surface of Fe–Al BDC was rapid enough to use to remove F^- from water with up to 45 min of contact time. In the case of the IPD model three stages were observed, as shown in Fig. 5d: an initial curved portion *i.e.*, for the liquid to Fe–Al BDC surface mass-transfer (phase-I), an intermediate linear portion for intra-particle diffusion, and a plateau part for the equilibrium stage (phase II).[65] The slope value for phase I was greater than for phase II in the IPD model and is tabulated in Table 1, which also confirmed that the rate of F^- adsorption was higher up to 45 min contact time onto the readily available adsorbing sites of Fe–Al BDC and got slower when proceeding towards saturation.[7] From the mass-transfer and Weber and Morris intra-particle diffusion (IPD) model, it could be said that the removal of F^- using Fe–Al BDC in an aqueous medium followed the proposed surface–boundary-layer mechanism, as shown in Fig. 8a. The proposed surface–boundary-layer mechanism is based on the electrostatic interactions[41] of the F^- anions onto the Fe–Al BDC surface. At lower pH, the Fe–Al BDC surface is positively charged and at higher pH the surface becomes negatively charged, as

shown in Fig. 5c-inset, *i.e.*, the ξ-potential study of Fe–Al BDC, and with the variation in the surface charge the F^- and Fe–Al BDC surface interactions are as shown in Fig. 8a.

In the XPS analyses of Fe–Al BDC prepared at 473 K for 70 h, the characteristic peaks for $Fe2p_{1/2}$, $Fe2p_{3/2}$, $Al2p_{3/2}$, O_{1s}, C_{1s} were observed at 728.88, 710.32, 712.45, 76.85, 534.14, and 286.86 eV, respectively,[66] as shown in Fig. 9A-a, but after the F^- adsorption the binding energies of the metal centers changed, as shown in Fig. 9A-b. From the XPS analyses, as shown in Fig. 9A-C of Fe–Al BDC before and after F^- adsorption, the chemisorption of F^- onto the trivalent hard-acid centers, *i.e.*, Fe^{3+} and Al^{3+}, has been perfectly confirmed. For $Al2p_{3/2}$ and $Fe2p_{3/2}$ the binding energy increased from 76.85 eV to 77.18 eV and from 710.32–712.45 eV to 714.24 eV, as shown in Fig. 9B and C, respectively, showing the affinity to form a metal–fluoride bond, leading to chemisorption of F^-. The formation of a new peak with a binding energy of 683.02 eV of F_{1s} (ref. 67) after F^- adsorption clearly emphasizes the chemisorption of F^- onto the Fe–Al BDC surface, as shown in Fig. 9A-b and 9D.

3.6.2. Mechanism of RhB photodegradation. The photodegradation of various water-soluble dyes using photocatalysts on solar/light irradiation occurs mainly *via* hydroxyl radical attack, direct oxidation by holes, or direct reduction by electrons.[52] To investigate the key role of these degradation mechanism pathways on the photocatalytic degradation of RhB using Fe–Al BDC, tests were performed using some suitable trapping agent/scavenger: *e.g.*, ethanol (EtOH) for holes, isopropyl alcohol for $OH^\bullet$, and $AgNO_3$ for electron trapping using 1 mmol L^{-1} of the corresponding solutions.[34] The % degradation was not significantly decreased in the presence of EtOH or $AgNO_3$, *i.e.*, the hole and electron scavengers, respectively, but in the presence of IPA, the $OH^\bullet$ scavenger, the % degradation decreased sharply from 92.11% to 20.35%, as shown in Fig. S19,† which indicates that the $OH^\bullet$ radical played a pivotal role in the photodegradation. The abundance of $OH^\bullet$ radicals required some time to become populated in the reaction medium to speed up the reaction, which was supported by the two-step kinetic model. The decolorization efficiency of RhB increased slowly from 27.48% to 56.25% ($k_1' = 0.05598\ min^{-1}$) up to 10 min after solar irradiation and speeded up after 10 min from 56.25% to 92.11% ($k_2' = 0.17137\ min^{-1}$), as shown in the UV profile (Fig. 6d), which supports the two-step kinetic model $\left(\frac{C_t^{RhB}}{C_0^{RhB}} = Be^{-k_1' t} + Ce^{-k_2' t}\right)$,[68] as shown in Fig. S20b† where the phase-II rate constant k_1' > the phase-I rate constant k_1'. The initial interaction of RhB with Fe–Al BDC can be considered as adsorption governed by electrostatic-interactions between the surface charge of the photocatalyst[69] at pH 7 as the pH_{ZPC} of Fe–Al BDC is 7.22, as shown in Fig. 5c-inset. As the population of $OH^\bullet$ increased and the activation of RhB occurred after solar irradiation, as shown in eqn (4)–(8), the degradation of RhB proceeded by attack by the $OH^\bullet$ radicals. Considering that the photodegradation of RhB was conducted in an aerated medium, eqn (6)–(8) occurred as the consumption of O_2 occurred[70] under solar irradiation to activate the RhB molecules to the excited state.[71] In general, the photodegradation of RhB proceeded *via* a three-step mechanism: *i.e.*, (i) de-ethylation, (ii) chromophore

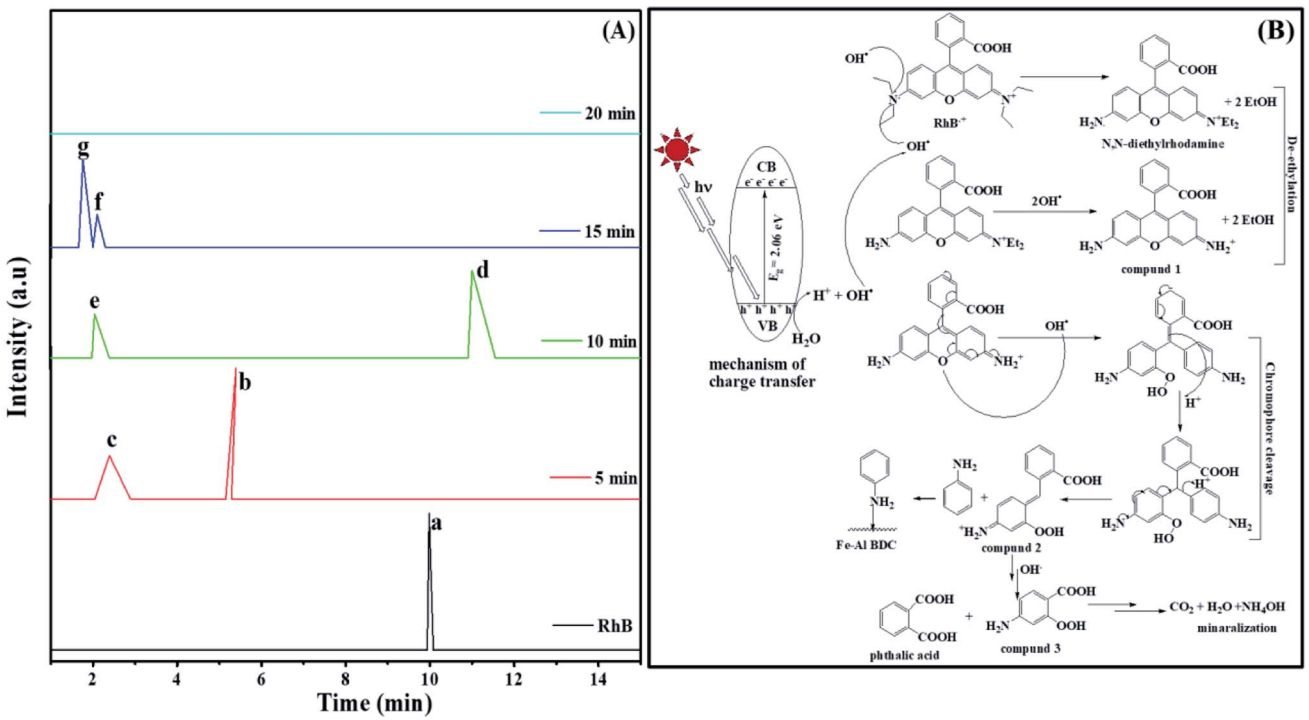

Fig. 10 (A) HPLC chromatograms of various aliquots taken after different time intervals during the degradation of 10^{-5} M RhB using 0.10 g/100 mL Fe–Al BDC (a. RhB, b. DER, c. compound **1**, d. aniline, e. compound **2**, f. phthalic acid, and g. compound **3**); (B) mechanism of the photodegradation of RhB using Fe–Al BDC prepared at 473 K for 70 h.

cleavage, and (iii) mineralization. The mineralization of RhB under solar irradiation using Fe–Al BDC was confirmed from the HPLC and TOC analyses, as shown in Fig. 10A and S21,† respectively.

$$\text{Fe–Al BDC} + h\nu \rightarrow \text{Fe–Al BDC}(e_{CB}^{-} + h_{VB}^{+}) \quad (4)$$

$$H_2O + h_{VB}^{+} \rightarrow H^{+} + OH^{\bullet} \quad (5)$$

$$\text{RhB} \xrightarrow{h\nu} \text{RhB*} \ \text{(excitation)} \quad (6)$$

$$\text{RhB*} + O_2 \rightarrow \text{RhB}^{\bullet+} + O_2^{\bullet-} \quad (7)$$

$$O_2^{\bullet-} + 2H^{+} \rightarrow 2OH^{\bullet} \quad (8)$$

The UV profile of the photodegradation of 10^{-5} (M) RhB, as shown in Fig. 6d, illustrated that RhB was degraded gradually with prolonged reaction time, showing a slight hypochromic shift, as clearly shown in Fig. S19a† (enlarged) indicating the formation of a series of *N*-de-ethylated/ethylated intermediates or cleavage of the conjugated chromophore structure of RhB in the photodegradation process[72] in a stepwise manner. Chen *et al.* also observed this type of phenomenon during the photodegradation of RhB under visible irradiation using a TiO_2/SiO_2 composite.[73] The HPLC analysis of the aliquots of this photodegradation process describes the formation of different types of products following mineralization, as $OH^{\bullet}$ attack, occurring under prolonged solar irradiation, as shown in Fig. 10A. In the first step, de-ethylation occurred, producing compound **1** (Fig. 10B), R_t = 2.40 min through *N*,*N*-diethylrhodamine (R_t = 5.40 min),[72] as shown in Fig. 10A-c. In the next step chromophore cleavage occurred by $OH^{\bullet}$ attack and proton (H^+) take-up (Fig. 10B) forming aniline (R_t = 11.02 min)[74] and compound **2** (R_t = 2.01 min) (Fig. 10A-e) and after some time the aniline was adsorbed onto the Fe–Al BDC surface, supported by the FTIR analysis, as discussed in Fig. S17.† After the chromophore cleavage (Fig. 10B), phthalic acid (R_t = 1.30 min)[72] and compound **3** (R_t = 1.12 min) were formed (Fig. 10A-g), and mineralization took place simultaneously, as shown in Fig. 10A and B. In the end, the HPLC profile of the last aliquot taken, parallel with the time axis, represents the mineralization of the RhB dye. This mechanism was also supported by measurements of the pH and other water parameters (conductance, salinity, resistivity, TDS, *etc.*), tabulated in Table S4,† where the increase in solution pH describes the formation of NH_4OH at the end of the reaction making the reaction mixture alkaline. Horikoshi *et al.*[75] used TiO_2, and Zhong He *et al.*[72] used Bi_2WO_6 under microwave irradiation for the degradation of RhB where this type of *N*-de-ethylation process was followed by benzenoid removal and opening-ring intermediates. But in the reported systems the degradation time was ~60 min, which is longer than in our process. This could be explained as in our process the chromophore cleavage and mineralization occurred simultaneously, which leads to a shorter time for degradation compared to the reported processes. The stability of Fe–Al BDC was confirmed by FTIR and XRD analyses after the photodegradation process where no characteristic change was observed, as shown in Fig. S17 and S22,† respectively.

In this work, the recycling of solvent used in this synthesis, *i.e.*, DMF, was also checked. The DMF collected from the first synthesis was successfully used twice to synthesize Fe–Al BDC, which was confirmed by the PXRD analysis as shown in Fig. S23.†

4. Conclusion

A 3D rod-like bimetallic MOF, abbreviated as Fe–Al BDC, with a large surface area of 120.255 $m^2\ g^{-1}$ was successfully synthesized *via* a solvothermal method using terephthalic acid as a linker. The newly synthesized Fe–Al BDC was used for the chemisorption of F^- and the photodegradation of various water-soluble organic dyes (RhB/MB) using solar irradiation at pH 7 for the first time, to the best of our knowledge. Monoclinic Fe–Al BDC was analyzed through PXRD and HRTEM studies and was thermally stable up to 300 °C, as confirmed by TGA analysis. The structural information, involving μ-oxo metal bonds, was confirmed *via* PXRD, FTIR, and Raman analyses. The presence of various defects in Fe–Al BDC was confirmed based on W–H plots, PL spectral analysis, and EPR studies. DMF used in the synthesis could be further reused for two cycles to prepare the same MOF, as confirmed by PXRD studies. The 3D rod-like structure was found based on FESEM analysis, and corresponding SAEDS and elemental mapping studies helped to establish the chemical composition, which was also confirmed *via* ICP analysis. The particle size and surface area followed the André relationship. The highest F^- removal efficiency was found to be 95.60% using 0.10 g/100 mL Fe–Al BDC for a contact time of 45 min, and it followed pseudo-second-order kinetics with a rate constant $k_2 = 1.07 \times 10^{-1}$ g min mg^{-1} at 30 °C and pH 7 and also obeyed the Langmuir and Freundlich adsorption isotherms. The chemisorption of F^- was confirmed based on FTIR and XPS analyses, and thermodynamics studies were done using the Van't Hoff method; negative thermodynamic parameters (ΔG^0, ΔH^0, and ΔS^0) were obtained, which indicated that adsorption was spontaneous, exothermic, and repeatable. The F^- adsorption mechanism followed a surface–boundary-layer mechanism, supported by the Weber and Morris interparticle-diffusion model and McKay *et al.* mass-transfer model, and this was also supported by ξ-potential analysis. Fe–Al BDC was also able to photodegrade RhB/MB at different concentrations (10^{-5}/10^{-4} M) under solar irradiation, and the proposed mechanism was supported by HPLC and spectral analysis. The photodegradation process followed mainly pseudo-first-order kinetics. The influence of co-ions (Cl^-, SO_4^{2-}, HCO_3^-, NO_3^-, PO_4^{3-}, *etc.*) was tested in relation to the F^- removal and photodegradation processes. The photodegradation percentages for RhB and MB degradation were >90% for both 10^{-5} and 10^{-4} M concentrations. Fe–Al BDC was reusable in studies for up to eight successive cycles for both processes. The mechanism of the photodegradation of RhB was controlled by $OH^{\bullet}$ attack, with the *in situ* generation of $OH^{\bullet}$ radicals in the aqueous medium. The photodegradation mechanism was established based on HPLC, UV-vis, and FTIR studies. Hence, porous, nanosized Fe–

Al BDC with a large surface area can be used as a potential material for F^- removal and the photodegradation of water-soluble organic dyes under solar irradiation for household and industrial purposes.

Conflicts of interest

On behalf of all authors, the corresponding author states that there are no conflicts of interest.

Acknowledgements

The authors would like to thank the Department of Science and Technology; Government of West Bengal vide project sanction no. 674/ST/P/S&T/15G/5/2016 dated 09/11/2016 for financial support and Department of Science and Technology, New Delhi, Government of India vide project sanction no. DST, SEED/TITE/2019/84 for financial support.

References

1 W. He, H-K. Kim, W. G. Wamer, D. Melka, J. H. Callahan and J.-J. Yin, Photogenerated Charge Carriers and Reactive Oxygen Species in ZnO/Au Hybrid Nanostructures with Enhanced Photocatalytic and Antibacterial Activity, *J. Am. Chem.Soc.*, 2014, **136**(2), 750–757.

2 P. Khare, A. Singh, S. Verma, A. Bhati, A. K. Sonker, K. M. Tripathi and S. K. Sonkar, Sunlight-Induced Selective Photocatalytic Degradation of Methylene Blue in Bacterial Culture by Pollutant Soot Derived Nontoxic Graphene Nanosheets, *ACS Sustainable Chem. Eng.*, 2018, **6**(1), 579–589.

3 P. Kumar, V. Bansal, Ki-H. Kim and E. E. Kwon, Metal-organic frameworks (MOFs) as futuristic options for wastewater treatment, *J. Ind. Eng. Chem.*, 2018, **62**, 130–145.

4 L. J. Murray, M. Dincă and J. R. Long, Hydrogen storage in metal–organic frameworks, *Chem. Soc. Rev.*, 2009, **38**, 1294–1314.

5 A. Chowdhury, M. K. Adak, A. Mukherjee, P. Dhak, J. Khatun and D. Dhak, A critical review on geochemical and geological aspects of fluoride belts, fluorosis and natural materials and other sources for alternatives to fluoride exposure, *J. Hydrol.*, 2019, **574**, 333–359.

6 S. Khan, A. Malik, *Environmental and Health Effects of Textile Industry Wastewater.* Environmental Deterioration and Human Health, 2013: pp. 55–71.

7 N. Zhang, X. Yang, X. Yu, Y. Jia, J. Wang, L. Kong, Z. Jin, B. Sun, T. Luo and J. Liu, Al-1,3,5-benzenetricarboxylic metal-organic frameworks: A promising adsorbent for defluoridation of water with pH insensitivity and low aluminum residual, *Chem. Eng. J.*, 2014, **252**, 220–229.

8 M. Mohapatra, S. Anand, B. K. Mishra, D. E. Giles and P. Singh, Review of fluoride removal from drinking water, *J. Environ. Manage.*, 2009, **91**, 67–77.

9 S. Chatterjee and S. De, Adsorptive removal of fluoride by activated alumina doped cellulose acetate phthalate (CAP) mixed matrix membrane, *Sep. Purif. Technol.*, 2014, **125**, 223–238.

10 S. S. Tripathy, J.-L. Bersillon and K. Gopal, Removal of fluoride from drinking water by adsorption onto alum-impregnated activated alumina, *Sep. Purif. Technol.*, 2006, **50**, 310–317.

11 S. Jain and R. V. Jayaram, Removal of fluoride from contaminated drinking water using unmodified and aluminium hydroxide impregnated blue lime stone waste, *Sep. Sci. Technol.*, 2009, **44**, 1436–1451.

12 L. M. Camacho, A. Torres, D. Saha and S. Deng, Adsorption equilibrium and kinetics of fluoride on sol-gel-derived activated alumina adsorbents, *J. Colloid Interface Sci.*, 2010, **349**, 307–313.

13 S. karmakar, J. Dechnik, C. Janiak and S. De, Aluminium fumarate metal-organic framework: A super adsorbent for fluoride from water, *J. Hazard. Mater.*, 2016, **303**, 10–20.

14 S. Malato, P. Fernandez-Ibanez, M. I. Maldonado, J. Blanco and W. Gernjak, Decontamination and Disinfection of Water by Solar Photocatalysis: Recent Overview and Trends, *Catal. Today*, 2009, **147**, 1–59.

15 T. F. Jiao, H. Zhao, J. Zhou, Q. Zhang, X. Luo, J. Hu, Q. Peng and X. Yan, The SelfAssembly Reduced Graphene Oxide Nanosheet Hydrogel Fabrication by Anchorage of Chitosan/Silver and its Potential Efficient Application Toward Dyes Degradation for Wastewater Treatments, *ACS Sustainable Chem. Eng.*, 2015, **3**(12), 3130–3139.

16 J.-J. Du, Y.-P. Yuan, J.-X. Sun, F.-M. Peng, X. Jiang, L.-G. Qiu, A.-J. Xie, Y.-H. Shen and J.-F. Zhu, New photocatalysts based on MIL-53 metal–organic frameworks for the decolorization of methylene blue dye, *J. Hazard. Mater.*, 2011, **190**, 945–951.

17 H. Ramezanalizadeh and F. Manteghi, Synthesis of a novel MOF/$CuWO_4$ heterostructure for efficient photocatalytic degradation and removal of water pollutants, *J. Cleaner Prod.*, 2018, **172**, 2655–2666.

18 M. R. Azhar, H. R. Abid, H. Sun, V. Periasamy, M. O. Tadé and S. Wang, One-pot synthesis of binary metal organic frameworks (HKUST-1 and UiO-66) for enhanced adsorptive removal of water contaminants, *J. Colloid Interface Sci.*, 2017, **490**, 685–694.

19 Y. Bian, N. Xiong and G. Zhu, Technology for the Remediation of Water Pollution: A Review on the Fabrication of Metal Organic Frameworks, *Processes*, 2018, **6**, 122.

20 B. Z. Ying Chen, Y. Liang, Y. Li and Li Jing, Preparation of CdS/g-C_3N_4/MOF composite with enhanced visible-light photocatalytic activity for dye degradation, *J. Solid State Chem.*, 2019, **274**, 32–39.

21 K.-T. Lee, X.-F. Chuah, Y.-C. Cheng and S.-Y. Lu, Pt coupled $ZnFe_2O_4$ nanocrystals as a breakthrough photocatalyst for Fenton-like processes - photodegradation treatments from hours to seconds, *J. Mater. Chem. A*, 2015, **3**, 18578–18585.

22 M. K. Adak, A. Sen, A. Mukherjee, S. Sen and D. Dhak, Removal of fluoride fron drinking water using highly efficient nano-adsorbent, Al(III)-Fe(III)-La(III) trimetallic oxide prepared by chemical route, *J. Alloys Compd.*, 2017, **719**, 460–469.

23 A. Mukherjee, M. K. Adak, A. Chowdhury and D. Dhak, Synthesis of Cost-effective Trimetallic Oxide Nanocatalysts

for the Reduction of Nitroarenes in Presence of $NaBH_4$ in an Aqueous Medium, *Curr. Catal.*, 2019, **8**, 41–55.

24 A. Mukherjee, M. K. Adak, P. Dhak and D. Dhak, A simple chemical method for the synthesis of Cu^{2+} engrafted $MgAl_2O_4$ nanoparticles: Efficient fluoride adsorbents, photocatalyst and latent fingerprint detection, *J. Environ. Sci.*, 2020, **88**, 301–315.

25 G. T. Vuong, M.-H. Pham and T. O. Do, Direct synthesis and mechanism of the formation of mixed metal Fe_2Ni-MIL-88B, *CrystEngComm*, 2013, **45**(15), 9694.

26 C. M. Navarathna, N. B. Dewage, A. G. Karunanayake, E. L. Farmer, F. Perez, E. B. Hassan, T. E. Mlsna and C. U. Pittman Jr, Rhodamine B Adsorptive Removal and Photocatalytic Degradation on MIL-53-Fe MOF/Magnetic Magnetite/Biochar Composites, *J. Inorg. Organomet. Polym. Mater.*, 2020, **30**, 214–229.

27 N. Liu, C. Jing, Z. Li, W. Huang, B. Gao, F. You and X. Zhang, Effect of synthesis conditions on the photocatalytic degradation of Rhodamine B of MIL-53 (Fe), *Mater. Lett.*, 2019, **237**, 92–95.

28 J. Y. Ying, J. B. Benziger and H. Gleiter, Photoacoustic infrared spectroscopy of nanoclusters Al_2O_3clusters and cluster-assembled solids, *Phys. Rev. B: Condens. Matter Mater. Phys.*, 1993, **48**, 1830–1836.

29 H.-T. T. Nguyen, V.-P. Dinh, Q.-A. N. Phan, V. A. Tran, V.-D. Doan, T. Lee and T. D. Nguyen, Bimetallic Al/Fe Metal-Organic Framework for highly efficient photo-Fenton degradation of rhodamine B under visible light irradiation, *Mater. Lett.*, 2020, **279**, 128482.

30 M. Barathi, A. Santhana Krishna Kumar, C. U. Kumar and N. Rajesh, Graphene oxide–aluminium oxyhydroxide interaction and its application for the effective adsorption of fluoride, *RSC Adv.*, 2014, **4**, 53711–53721.

31 G. T. Vuong, M.-H. Pham and T. O. Do, Synthesis and engineering porosity of a mixed metal Fe_2Ni MIL-88B metal-organic framework, *Dalton Trans.*, 2013, **42**, 550–557.

32 X. Feng, H. Chen and F. Jiang, In-situ ethylenediamine-assisted synthesis of a magnetic iron-based metal–organic framework MIL-53(Fe) for visible light photocatalysis, *J. Colloid Interface Sci.*, 2017, **494**, 32–37.

33 M. André, M. E. Malmström and I. Neretnieks, Specific surface area determinations on intact drillcores and evaluation of extrapolation methods for rock matrix surfaces, *J. Contam. Hydrol.*, 2009, **110**, 1–8.

34 L. Renuka, K. S. Anantharaju, Y. S. Vidya, H. P. Nagaswarupa, S. C. Prashantha, S. C. Sharma, H. Nagabhushana and G. P. Darshan, A simple combustion method for the synthesis of multi-functional ZrO_2/CuO nanocomposites: Excellent performance as Sunlight photocatalysts and enhanced latent fingerprint detection, *Appl. Catal., B*, 2017, **210**, 97–115.

35 G. Lucoysky, C. L. Hinkle, C. C. Fulton, N. A. Stoute, H. Seo and J. Lüning, Intrinsic nanocrystalline grain-boundary and oxygen atom vacancy defects in ZrO_2 and HfO_2, *Radiat. Phys. Chem.*, 2006, **75**(11), 2097–2101.

36 F. A. Kröger and H. j. Vink, *Relations between the Concentrations of Imperfections in Crystalline Solids.* Solid State Physics, 1956, pp. 307–435.

37 C. Gionco, M. C. Paganini, E. Giamello, R. Burgess, C. DiValentin and G. Pacchioni, Paramagnetic Defects in Polycrystalline Zirconia: An EPR and DFT Study, *Chem. Mater.*, 2013, **25**, 2243–2253.

38 Y. Liu, Y. Zhu, J. Xu, X. Bai, R. Zong and Y. Zhu, Degradation and Mineralization Mechanism of Phenol by $BiPO_4$ Photocatalysis Assisted with H_2O_2, *Appl. Catal., B*, 2013, **142–143**, 561–567.

39 Z. Klencsár and Z. Köntös, EPR Analysis of Fe^{3+} and Mn^{2+} Complexation Sites in Fulvic Acid Extracted from Lignite, *J. Phys. Chem. A*, 2018, **122**(12), 3190–3203.

40 C. Phadnis, D. Inamdar, I. Dubenko, A. Pathak, N. Ali and S. Mahamuni, Ferromagnetic ZnO nanocrystals and Al-induced defects, *J. Appl. Phys.*, 2011, **110**, 114316.

41 A. Mukherjee, M. K. Adak, S. Upadhyay, J. Khatun, P. Dhak, S. Khawas, U. K. Ghorai and D. Dhak, Efficient Fluoride Removal and Dye Degradation of Contaminated Water Using Fe-Al-Ti Oxide Nanocomposite, *ACS Omega*, 2019, **4**, 9686–9696.

42 M. K. Adak, A. Sen, A. Mukherjee, S. Sen and D. Dhak, Removal of fluoride from drinking water using highly efficient nano-adsorbent, Al(III)-Fe(III)-La(III) trimetallic oxide prepared by chemical route, *J. Alloys Compd.*, 2017, **719**, 460–469.

43 A. Mukherjee, M. K. Adak, A. Chowdhury and D. Dhak, Synthesis of cost effective trimetallic oxide nano catalysts for the reduction of nitroarenes in presence of $NaBH_4$ in aqueous medium, *Curr. Catal.*, 2019, **8**(1), 41–55.

44 M. Yazdanbakhsh, I. Khosravi, E. K. Goharshadi and A. Youssefi, Fabrication of nanospinel $ZnCr_2O_4$ using sol–gel method and its application on removal of azo dye from aqueous solution, *J. Hazard. Mater.*, 2010, **184**, 684–689.

45 A. Ghosh and G. Das, Green synthesis of a novel water-stable Sn(II)-TMA metal–organic framework (MOF): Efficient adsorbent for fluoride in the aqueous medium in the wide pH range, *New J. Chem.*, 2020, **44**, 1354–1361.

46 K.-Y. A. Lin, Y.-T. Liu and S.-Y. Chen, Adsorption of fluoride to UiO-66-NH_2 in water: Stability, kinetic, isotherm and thermodynamic studies, *J. Colloid Interface Sci.*, 2016, **461**(1), 79–87.

47 T. L. Tan, P. A/P Krusnamurthy, H. Nakajima and S. A. Rashid, Adsorptive, kinetics and regeneration studies of fluoride removal from water using zirconium-based metal organic frameworks, *RSC Adv.*, 2020, **10**, 18740–18752.

48 M. H. Saghi, B. Chabot, S. Rezania, M. Sillanpää, A. A. Mohammadi, M. Shams and A. Alahabadi, Water-stable zirconium and iron-based metal–organic frameworks (MOFs) as fluoride scavengers in aqueous medium, *Sep. Purif. Technol.*, 2021, **270**, 118645.

49 A. Sarkar, A. Adhikary, A. Mandal, T. Chakraborty and D. Das, Zn-BTC MOF as an Adsorbent for Iodine Uptake and Organic Dye Degradation, *Cryst. Growth Des.*, 2020, **20**(12), 7833–7839.

50 M. Zhang, L. Wang, T. Zeng, Q. Shang, H. Zhou, Z. Pan and Q. Cheng, Two pure MOF-photocatalysts with readily preparation for the degradation of methylene blue dye under visible light, *Dalton Trans.*, 2018, **47**, 4251–4258.

51 S. K. Swain, T. P., V. K. Singh, U. Jha, R. K. Patel and R. K. Dey, Kinetics, equilibrium and thermodynamic aspects of removal of fluoride from drinking water using meso-structured zirconium phosphate, *Chem. Eng. J.*, 2011, **171**, 1218–1226.

52 T. A. Saleh and V. K. Gupta, Functionalization of tungsten oxide into MWCNT and its application for sunlight-induced degradation of rhodamine B, *J. Colloid Interface Sci.*, 2011, **362**, 337–344.

53 N. Serpone, R. Terzian, H. Hidaka and E. Pelizzetti, Ultrasonic Induced Dehalogenation and Oxidation of 2-, 3-, and 4-Chlorophenol in Air-Equilibrated Aqueous Media. Similarities with Irradiated Semiconductor Particulates, *J. Phys. Chem.*, 1994, **98**, 2634–2640.

54 G. E. Brown, V. E. Henrich, W. H. Casey, D. L. Clark, C. Eggleston, A. Felmy, D. Wayne Goodman, M. Grätzel, G. Maciel, M. I. McCarthy, K. H. Nealson, D. A. Sverjensky, M. F. Toney and J. M. Zachara, Metal Oxide Surfaces and Their Interactions with Aqueous Solutions and Microbial Organisms, *Chem. Rev.*, 1999, **99**(1), 77–174.

55 M. Massoudinejad, M. Ghaderpoori, A. Shahsavani and M. M. Amini, Adsorption of fluoride over a metal organic framework Uio-66 functionalized with amine groups and optimization with response surface methodology, *J. Mol. Liq.*, 2016, **221**, 279–286.

56 L. Lv, J. He, M. Wei, D. G. Evans and X. Duan, Factors influencing the removal of fluoride from aqueous solution by calcined Mg-Al-CO_3 layered double hydroxides, *J. Hazard. Mater.*, 2006, **133**, 119–128.

57 H. Zhu, R. Jiang, L. Xiao, Y. Chang, Y. Guan, X. Li and G. Zeng, Photocatalytic decolorization and degradation of Congo Red on innovative crosslinked chitosan/nano-CdS composite catalyst under visible light irradiation, *J. Hazard. Mater.*, 2009, **169**, 933–940.

58 Z. Hasan, E.-J. Choi and S. H. Jhung, Adsorption of naproxen and clofibric acid over a metal–organic framework MIL-101 functionalized with acidic and basic groups, *Chem. Eng. J.*, 2013, **219**, 537–544.

59 M. Wang, L. Yang, C. Guo, X. Liu, L. He, Y. Song, Q. Zhang, X. Qu, H. Zhang, Z. Zhang and S. Fang, Bimetallic Fe/Ti-Based Metal-Organic Framework for Persulfate-Assisted Visible Light Photocatalytic Degradation of Orange II, *Chemistry Select*, 2018, **3**, 3664–3674.

60 A. Mohammad, G. K. C. Low and W. M. Ralph, Effects of common inorganic anions on rates of photocatalytic oxidation of organic carbon over illuminated titanium dioxide, *J. Phys. Chem. A*, 1990, **94**, 6820–6825.

61 S. P. Kamble, S. Jagtap, N. K. Labhsetwar, D. Thakare, S. Godfrey, S. Devotta and S. S. Rayalu, Defluoridation of drinking water using chitin, chitosan and lanthanum-modified chitosan, *Chem. Eng. J.*, 2007, **129**, 173–180.

62 A. Mukherjee, A. Chowdhury, M. K. Adak, J. Khatun, P. Dhak and D. Dhak, Fluoride adsorption and photoreduction of Cr(VI) using heterogeneous Al^{3+} modified mine-waste, an *in situ* approach, *J. Environ. Chem. Eng.*, 2020, **8**, 103759.

63 W. H. Cheung, Y. S. Szeto and G. McKay, Intraparticle diffusion processes during acid dye adsorption onto chitosan, *Bioresour. Technol.*, 2007, **98**, 2897–2904.

64 H. Tran and F. A. Roddick, Comparison of chromatography and desiccant silica gel for the adsorption of metal ions. I: Adsorption and kinetics, *Water Res.*, 1999, **33**, 2992–3000.

65 A. A. M. Daifullah, S. M. Yakout and S. A. Elreefy, Adsorption of fluoride in aqueous solutions using $KMnO_4$-modified activated carbon derived from steam pyrolysis of rice straw, *J. Hazard. Mater.*, 2007, **147**, 633–643.

66 R. Wang, H. Xu, K. Zhang, S. Wei and D. Wu, High-quality Al@Fe-MOF prepared using Fe-MOF as a micro-reactor to improve adsorption performance for selenite, *J. Hazard. Mater.*, 2019, **364**, 272–280.

67 X. Dou, D. Mohan, C. U. Pittman Jr and S. Yang, Remediating fluoride from water using hydrous zirconium oxide, *Chem. Eng. J.*, 2012, **198–199**, 239–245.

68 S. J. M. Nassar, C. Wills and A. Harriman, Inhibition of the Photobleaching of Methylene Blue by Association with Urea, *ChemPhotoChem*, 2019, **3**(10), 1042–1049.

69 M. C. Fernández de Cordoba, J. Matosa, R. Montaña, P. S. Poon, S. Lanfredi, F. R. Praxedes, J. C. Hernández-Garrido, J. J. Calvino, E. Rodríguez-Aguado, E. Rodríguez-Castellón and C. O. Ania, Sunlight photoactivity of rice husks-derived biogenic silica, *Catal. Today*, 2019, **328**, 125–135.

70 J. Hong, C. Sun, S. G. Yang and Y. Z. Liu, Photocatalytic degradation of methylene blue in TiO_2 aqueous suspensions using microwave powered electrodeless discharge lamps, *J. Hazard. Mater.*, 2006, **133**, 162–166.

71 H. B. Fu, C. Pan, W. Q. Yao and Y. F. Zhu, Visible-light-induced degradation of rhodamine B by nanosized Bi_2WO_6, *J. Phys. Chem. B*, 2005, **109**, 22432–22439.

72 Z. He, C. Sun, S. Yang, Y. Ding, H. He and Z. Wang, Photocatalytic degradation of rhodamine B by Bi_2WO_6 with electron accepting agent under microwave irradiation: Mechanism and pathway, *J. Hazard. Mater.*, 2009, **162**, 1477–1486.

73 F. Chen, J. Zhao and H. Hidaka, Int. Highly selective deethylation of rhodamine B: adsorption and photooxidation pathways of the dye on the TiO_2/SiO_2 composite photocatalyst, *J. Photoenergy*, 2003, **5**, 209–217.

74 Y. Li, F. Wang, G. Zhou and Y. Ni, Aniline degradation by electrocatalytic oxidation, *Chemosphere*, 2003, **53**(10), 1229–1234.

75 S. Horikoshi, A. Saitou, H. Hidaka and N. Serpone, Environmental remediation by an integrated microwave/UV illumination method. V. Thermal and nonthermal effects of microwave radiation on the photocatalyst and on the photodegradation of rhodamine-B under UV/Vis radiation, *Environ. Sci. Technol.*, 2003, **37**, 5813–5822.